

UC Berkeley

UC Berkeley Electronic Theses and Dissertations

Title

Tissue Magnetic Susceptibility Matched Pyrolytic Graphite Foam for Improved MRI

Permalink

<https://escholarship.org/uc/item/9pd0r56m>

Author

Lee, Gary Chiaray

Publication Date

2011

Peer reviewed|Thesis/dissertation

Tissue Magnetic Susceptibility Matched Pyrolytic Graphite Foam for Improved MRI

By

Gary Chiaray Lee

A dissertation submitted in partial satisfaction of the

Requirements for the degree of

Joint Doctor of Philosophy
with University of California, San Francisco

in

Bioengineering

in the

Graduate Division

of the

University of California, Berkeley

Committee in charge:

Professor Steven Conolly, Chair
Professor John Kurhanewicz
Professor Michael Silver

Fall 2011

Abstract

Tissue Magnetic Susceptibility Matched Pyrolytic Graphite Foam for Improved MRI

by

Gary Chiaray Lee

Joint Doctor of Philosophy in Bioengineering
with University of California, San Francisco

and

University of California, Berkeley

Professor Steven Conolly, Chair

In MRI, a powerful and uniform static B_0 field is responsible for image signal and contrast. However, regions of different magnetic susceptibilities in the static field give rise to field inhomogeneities that cause image artifacts. For example, air and tissue interfaces for a patient in a MRI study induce up to ± 5 ppm static B_0 field perturbations within the patient. Unfortunately shim coils are too large to compensate for the very steep field variations found near the breast, cervical spine, shoulders, occipital lobe, and other regions of the body. Many MRI applications are vulnerable to B_0 inhomogeneity, including robust fat suppression, which requires better than ± 1 ppm homogeneity.

To address this challenge, we have developed a flexible, conforming composite foam with magnetic susceptibility matched to human tissue. We surround the region with enough matching material to move the field gradients *outside* of the body where they cannot cause MRI artifacts. Our matching material is a pyrolytic graphite (PG) composite foam. It has many advantages over existing matching agents: it is lightweight; it adds no noise; and it is safe to embed receiver coils within the PG foam.

In this thesis, we propose theory that describes the magnetic susceptibility matching properties of composite PG foam. We show experimental proof of concept susceptibility matching and safety in phantom experiments. We also experimentally demonstrate that PG foam cushions improve the B_0 field uniformity to the critical threshold of ± 1 ppm in both phantoms and in the neck of 6 normal volunteers at 3T. The tissue susceptibility matched PG foams consistently mitigate signal drop out, improve image SNR, and enable far more robust frequency selective fat suppression in T_1 -weighted FLASH images in volunteers. PG foam has many practical applications in MR applications that require a pristine B_0 field.

To my Family and Friends.

Acknowledgements

My time in the Berkeley/UCSF Bioengineering Graduate Group has been an extended, but rewarding series of research, experiences, and adventures. I have shared this journey with so many wonderful and caring people, without whom I would not be where I am today. I have been at Berkeley for a very^M long time, so I have many^N people to thank, where M and N are large integers.

I would first like to thank my advisor, Steven Conolly. This work would not have been possible without his unfailing support and guidance. I count myself extremely lucky to have had an advisor like Steve, who is both a mentor and a friend. In addition to helping me become a better engineer and researcher, Steve gave me the freedom and encouragement to explore all the great things in the Bay area, so that I would have the opportunities to develop both professionally and as an individual.

I have been very fortunate to have the opportunity to come to lab each day and work with amazing people who are not only my colleagues, but my friends as well. I would like to thank Patrick Goodwill, Emine Saritas, Laura Croft, Bo Zheng, Kuan Lu, and Justin Konkle for all their help, assistance, and good cheer in lab. I especially want to thank Patrick and Emine for always having the time to teach me something new and for keeping my spirits up and encouraging me in the final, toughest stages of this process. Patrick and I started in the lab at the same time, and his energy, knowledge, and accomplishments never cease to amaze me. Patrick never failed to have a good answer or idea whenever I had a question or reached an impasse in my research or in my personal life. On the other hand, Emine joined the lab in my last year or so, and always had the ability point out something new and valuable in my data just by glancing over my shoulder. In addition, I truly appreciate the many lessons on Turkish culture and modern day techie gadgets that she gave me. I also want to thank Caroline Jordan at Stanford for her efforts in our first collaborative PG foam experiments...no one should be that cheerful during 4am scan sessions!

Much of the credit for the data I present in this work should go to the undergraduate researchers who have worked on this project: Pamela Tiet, Jeff McCormick, Carlos Ruiz, Kevin Phuong, Margaret Wei, Rachana Patel, and Alex Chen. Special thanks go to Pam, Jeff, and Carlos for all the late night scanning and tedious prototyping of the pyrolytic graphite foams and molds...and for all the lab pranks and hijinks to keep up our collective morale.

I would like to express my gratitude to the wonderful staff in the Bioengineering office: Rebecca Pauling, Amy Robinson, Jennifer Teverbaugh, Catherine Ocampo, Tere Falciglia, Mona Williams, Pamela Reynolds, Allison Rath, Cindy Manly-Fields, and Lindsay Hegg. In an ocean of Berkeley bureaucracy, they are collectively an island of efficiency, helpfulness, and kindness.

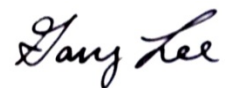
I have many faculty members that I need to thank for their encouragement and contributions to my academic career throughout the years. I want to thank my dissertation committee members, John Kurhanewicz (UCSF), Michael Silver (Berkeley), Nola Hylton (UCSF), and Mark D'Esposito (Berkeley), for providing helpful direction, insights, and encouragement during my research. I want to thank Brian Hargreaves and Greig Scott at Stanford University for their help and assistance in our collaborative efforts. I have learned so much from each of them.

At the Berkeley Brain Imaging Center, I would like to thank Ben Inglis, Daniel Sheltraw, Rick Redfern, and Miguel Perez for all their help with the 3T Siemens and 4T Varian MRI scanners. Without their efforts none of this research would have been possible. I especially want to thank Ben for his generosity with his time and willingness to try any and all interesting new research directions at a moment's notice.

I have lived in the same apartment complex since starting at Berkeley, moving only once...displacing myself ten feet downstairs from the same room in the upper unit to the corresponding one in the lower unit. I feel lucky to have had such a stable and wonderful living situation and I want to thank Matthew Chown, Justyn Jaworski, Samitha Samaranayake, John Pierson, and Nate Tom for being both roommates and friends over the many years. I especially appreciate that they let me occupy the kitchen and experiment constantly with no complaints!

There are so many wonderful friends that I have met during my time here, that I am afraid to attempt to thank them all individually, lest I leave someone out accidentally in my haste to finish this thesis. To all my friends, thank you for being there for me through good times and bad, and for indulging me in all my food and non-food adventures. I especially want to thank Randall Janairo, Melanie Prasol, Adrienne Higa, Anchi Tsou, Manu and Erica Seth, Karl Saldanha, and Jennifer Luu for always listening and helping when I needed it and for enjoying the best of times with me as well.

Last but certainly not least, I want to express my gratitude to my family for all their unconditional love and support. Mom, Dad, and Jenny...**Thank you!** My parents are truly my greatest inspirations. I cannot even imagine being able to even read a scientific paper in another language, much less having a career and raising a family in a foreign country. I am truly blessed that my parents worked so hard so that I would have the opportunities and encouragements in life to pursue my passions at so many institutions and in so many different things. Anytime I am feeling down, I just remember how lucky I truly am to have my parents and sister in my life, and all my worries seem inconsequential. I hope I will continue to make them proud as I continue my career.



Gary Lee
Berkeley
December 16th, 2011

Contents

Chapter 1: Introduction	1
1.1 Historical Notes	2
1.2 Motivation.....	2
1.3 Outline.....	2
Chapter 2: Preliminaries.....	4
2.1 Introduction.....	4
2.2 MRI Basics.....	4
2.2.1 The MR Signal.....	4
2.2.2 Intrinsic Contrast Mechanisms	6
2.2.3 MR Image Formation.....	6
2.3 Magnetic Susceptibility	8
2.4 Common Susceptibility Artifacts.....	9
2.5 B_0 Field Mapping.....	11
Chapter 3: Pyrolytic Graphite Foam Magnetic Susceptibility Matching Theory ..	14
3.1 Introduction.....	14
3.2 Pyrolytic Graphite.....	15
3.3 Composite Bulk Magnetic Susceptibility	15
3.4 Composite Electrical Conductivity	17
3.5 Quality Factor	18
3.6 RF Power Deposition.....	19
Chapter 4: Proof of Concept and Safety Testing	21
4.1 Introduction.....	21
4.2 Methods.....	23
4.2.1 PG Foam Construction.....	23
4.2.2 Phantom MRI Field Maps.....	23
4.2.3 Echo Planar Imaging with PG Foam	24
4.2.4 PG Foam Safety and RF Compatibility Testing	24
4.2.5 PG Foam Modifications.....	25
4.3 Results.....	25
4.3.1 PG Foam and MRI Phantom Images	25
4.3.2 PG Foam Conductivity	28
4.3.3 PG Foam Heating.....	29
4.3.4 Field Maps of Modified PG Foams	30
4.4 Discussion	32
Chapter 5: Frequency Selective Fat Suppression	36
5.1 Introduction.....	36
5.2 Methods.....	37
5.2.1 PG Foam Construction and SNR	37
5.2.2 Frequency Selective Fat Suppression in Phantoms and <i>In Vivo</i>	39

5.2.3 Data Processing.....	41
5.3 Results.....	41
5.3.1 PG Foams and SNR	41
5.3.2 Fat Phantom Field Maps and Fat Suppression.....	42
5.3.3 <i>In Vivo</i> Field Maps and Fat Suppression	45
5.4 Discussion.....	48
5.4.1 Alternative Methods of Fat Suppression.....	48
5.4.2 Static Field Shimming.....	49
5.4.3 PG Foam Air Gaps and Compression Tolerance.....	49
5.4.4 Conclusions.....	50
Chapter 6: Future Applications.....	51
6.1 Introduction.....	51
6.2 MRI in the Extremities.....	51
6.2.1 Motivation.....	51
6.2.2 Methods.....	51
6.2.3 Results.....	52
6.2.4 Brief Summary.....	54
6.3 PG Foam Pellets.....	55
6.3.1 Motivation.....	55
6.3.2 Methods.....	55
6.3.3 Results.....	55
6.3.4 Brief Summary.....	57
6.4 Industrial Manufacturing	57
6.4.1 Motivation.....	57
6.4.2 Methods.....	57
6.4.3 Results.....	58
6.4.4 Brief Summary.....	59
6.5 Embedded RF Coils	59
Chapter 7: Conclusions	61
7.1 Summary	61
7.2 Future Work	61
Bibliography	64

List of Figures

1.1 Representative MR images of the head	1
2.1 MRI spin polarization	5
2.2 Acquisition of the MR signal	5
2.3 Spatial encoding with linear gradients	7
2.4 Gradient recalled echo pulse sequence diagram	7
2.5 Simulated field map of an infinitely long cylinder perpendicular to the B_0 field.....	9
2.6 Example of an image distortion artifact.....	10
2.7 Examples of susceptibility induced artifacts.....	11
2.8 Examples of field maps.....	13
3.1 Concept diagram of a passive magnetic susceptibility matching	14
3.2 Magnetic susceptibility anisotropy of pyrolytic graphite crystals	15
3.3 Conceptual example of passive magnetic susceptibility matched PG foam	16
4.1 Concept diagram of tissue susceptibility matched pyrolytic graphite	22
4.2 Examples of PG foams.....	26
4.3 PG foam magnetic susceptibility matching proof of concept.....	26
4.4 Tolerance in target PG volume fraction in PG foams	27
4.5 Improvement of field maps and EPI images using PG foams	28
4.6 4T Q measurements	29
4.7 Direct heating measurements at 3T.....	29
4.8 Custom diamagnetic plasticizer reduces target PG volume fraction	30
4.9 Examples of 44 and 100 μm median diameter PG particles.....	31
4.10 Experimental field maps for PG foams made with 100 μm particles.....	31
5.1 Examples of anatomical 3D mold designs.....	38
5.2 Prototype 3D neck mold design.....	38
5.3 Foams used in SNR and posterior neck experiments.....	42
5.4 Simulated field maps and histograms of susceptibility phantoms	43
5.5 Experimental field maps and histograms for susceptibility phantoms	44
5.6 Experimental fat suppression images for susceptibility phantoms	44
5.7 Examples of global and local shim volumes.....	45
5.8 Experimental field maps and histograms in the cervical spine.....	46
5.9 Experimental fat suppression images in the cervical spine	47
5.10 Increased robustness of frequency selective fat suppression using PG foams	48
6.1 Anatomical molds of the hand and foot.....	52
6.2 Prototype PG foam ankle boot.....	53
6.3 Experimental field maps of the foot.....	53
6.4 Experimental fat suppression images of the foot.....	54
6.5 Experimental field maps of the hand	54
6.6 Example of PG foam pellets	56

6.7 Experimental field maps of 3.5-6.0% PG foam pellets	56
6.8 Experimental field maps and EPI images of compressed 3.5% PG foam pellets.....	57
6.9 Prototype foams from Mantec Services, Inc.....	58
6.10 Experimental field maps of 1.5% Mantec PG foams.....	58
6.11 Experimental field maps of 4.5% Mantec PG foams.....	59
6.12 Prototype PG foam cushion for use with Sentinelle breast MRI table	60

List of Tables

2.1 Analytic solutions for field perturbations due to common shapes.....	9
4.1 Experimental field homogeneity metrics for 100 μm PG foam phantoms	32
5.1 Experimental field homogeneity metrics for posterior neck volunteer study	46

Chapter 1

Introduction

Magnetic Resonance Imaging (MRI) is a powerful imaging modality that has come into widespread use in radiology with nearly 40 million annual scans in the United States (1). Along with x-ray, computed tomography (CT), ultrasound, and nuclear medicine, MRI provides the ability to non-invasively visualize internal structures in the human body. MRI is often used to image the central nervous system and the musculoskeletal system.

Advantages of MRI include the lack of harmful ionizing radiation, superior soft tissue contrast, and flexibility in generating image contrast. MRI contrast is sensitive to a wide range of tissue properties and can acquire image volumes and cross-sections in arbitrary sizes and orientations (2). For example, representative images in Fig 1.1 demonstrate the excellent spatial resolutions and anatomical details possible with MRI. In addition to anatomical imaging, MRI can also provide information about metabolic processes and spectroscopic content. However, a significant drawback of conventional MRI is the expensive and specialized hardware and electronics required, including an extremely strong magnet. Other disadvantages are weak signal to noise ratio (SNR), relatively slow imaging times, and patient motion, which makes imaging in regions of the body such as the abdomen very difficult (3).

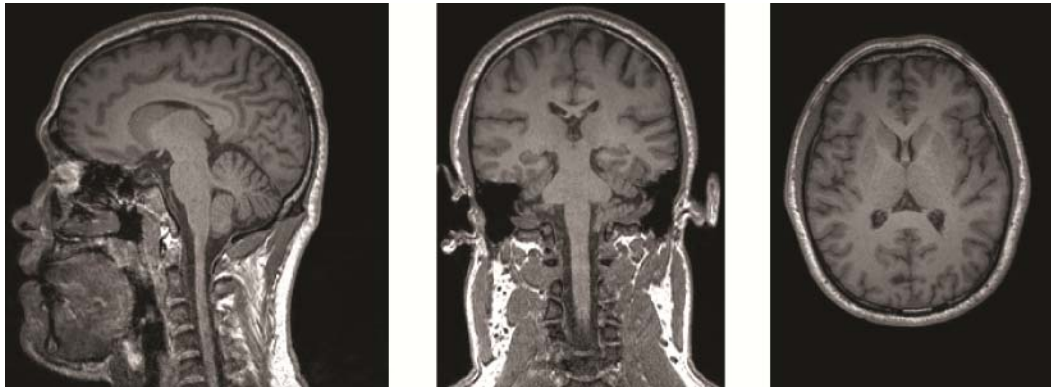


Fig 1.1: Representative sagittal, coronal, and axial MR images of the head (1 mm resolution).

MRI takes advantage of the property of nuclear magnetic resonance (NMR) to generate images of certain nuclei in the body. First, a powerful, static magnetic field, known as the B_0 field, is utilized to align the nuclei in the body. The most commonly imaged nucleus is the proton in hydrogen due to its abundance in the tissue in the form of water. Once aligned, the spins are then manipulated by a radiofrequency (RF) field at the resonant frequency of the spins, known as the Larmor frequency, in a manner which causes the rotating spins to induce an electromotive force in the receiver coils. Finally, additional magnetic field gradients enable spatial encoding of the spins and allow for the arbitrary imaging of volumes and cross-sections.

1.1 Historical Notes

Following the Stern-Gerlach experiments in the 1920's, which demonstrated that particles possess intrinsic angular spin momentum, Isidor Rabi first described the phenomenon of NMR in 1938 (4), for which he received the Nobel Prize in Physics in 1944. Next, Felix Bloch and Edward Purcell shared the Nobel Prize in Physics in 1952 for independently observing the precession behavior of protons in strong magnetic fields in 1946 (5,6). Then in 1973, Peter Mansfield pioneered the mathematics for analyzing MRI signals and Paul Lauterbur demonstrated the first MR image using linear gradient fields (7,8). In 2003, they shared the Nobel Prize in Medicine for their work. After the development and proliferation of clinical imaging scanners following the 1980's, MRI has evolved into a preferred method for non-invasive imaging of soft tissues, especially in regions that do not suffer from excessive cardiac and respiratory motion, such as the head, spine, and joints.

1.2 Motivation

Field gradients arising from air and tissue interfaces, such as those near the skin, can result in inhomogeneities in the MRI B_0 static field due to the mismatch in magnetic susceptibilities. These perturbations can lead to common imaging artifacts, including intravoxel dephasing, blurring, and voxel shifts, especially with typical gradient echo sequences. These perturbations typically increase at higher field strength and are also commonly seen in extremity MR imaging, such as spine, breast, wrist, knee, and foot MRI. Thus it can be difficult to obtain reliable MRI data near these interfaces, compromising the ability to fully capitalize on the potential of high field MRI for robust extremity imaging. Hence there is a need to remove or minimize these field inhomogeneities.

1.3 Outline

This thesis presents the development of a passive tissue magnetic susceptibility matching material for improving B_0 static field inhomogeneities due to air and tissue interfaces for MRI studies near the skin. Specifically, the theory, data acquisition, image processing, and analysis methods corresponding to the use of prototype composite PG foams are presented. PG foams are used to meet field homogeneity requirements for frequency selective fat suppression MRI techniques. Other applications that may benefit from susceptibility matching PG foams are also discussed.

This thesis is organized as follows:

Chapter 2: Preliminaries

An overview of MRI basics, magnetic susceptibility, B_0 field mapping techniques, and susceptibility-induced artifacts in MRI is presented in this chapter.

Chapter 3: Pyrolytic Graphite Foam Magnetic Susceptibility Matching Theory

The theory governing passive susceptibility matching in MRI using composite foams doped with PG particles is introduced. Conductivity, signal to noise (SNR), and safety considerations of the PG foams are particularly emphasized.

Chapter 4: Proof of Concept and Safety Testing

Prototype PG foams are presented to demonstrate proof of concept passive susceptibility matching in MRI. Demonstrated in phantoms, the PG foams reduce B_0 static field perturbations near previously mismatched susceptibility interfaces. PG foams are also shown to be non-conductive and safe for patient use.

Chapter 5: Frequency Selective Fat Suppression

MRI studies often use frequency selective fat suppression (fat saturation) techniques to eliminate fat signals that may obscure tissue contrast. This technique requires an extremely uniform static magnetic field that is often difficult to achieve due to field perturbations arising from typical air and tissue interfaces in the body. In this chapter, the use of PG foams to improve the robustness of fat saturation is demonstrated in phantoms and in the posterior neck/cervical spine region.

Chapter 6: Future Applications

The increased robustness to B_0 static field homogeneity from the use of PG foams is relevant to many MRI applications. In this chapter, preliminary data motivating new applications and PG foam susceptibility matching techniques are presented and discussed.

Chapter 7: Summary and Conclusions

The techniques presented in the previous chapters to improve passive tissue susceptibility matching using pyrolytic graphite are summarized in this chapter.

Chapter 2

Preliminaries

2.1 Introduction

This chapter briefly reviews basic concepts of MRI, including the generation of the MR signal, intrinsic contrast mechanisms, MR image formation, magnetic susceptibility, common susceptibility artifacts, and the basic principles of B_0 field mapping. This thesis is not intended to be a comprehensive review of MRI and its related applications. For a more comprehensive treatment of MR physics, imaging, and systems, excellent textbooks are available, including those by Haacke et al (2) and Nishimura (3). An in-depth review of magnetic susceptibility and its role in MRI can be found in Schenck's seminal paper (9).

2.2 MRI Basics

2.2.1 The MR Signal

Atoms with an odd total number of protons and/or neutrons exhibit the intrinsic quantum mechanical property known as angular momentum or *nuclear spin*. Examples in the body include hydrogen (1H), carbon (^{13}C), fluorine (^{19}F), phosphorous (^{31}P), and sodium (^{23}Na). Hydrogen protons dominate in the body because the body is essentially composed of water. The nuclear spin gives a net magnetic moment (μ) to each nucleus, but these are randomly oriented in space in the absence of a magnetic field. In a magnetic field, the spins are polarized. Once tipped away from the magnetic field, the spins precess about that field at a specific frequency, the *Larmor frequency* (ω_0), which depends linearly on the field magnitude and the gyromagnetic ratio (γ) for that particular nucleus. In MRI, the powerful polarizing static field is known as the B_0 field, which also gives the resonant frequency

$$\omega_0 = \gamma B_0. \quad (\text{Eq. 2.1})$$

In the B_0 field, the spins either align or anti-align with the field, with a slight thermodynamically driven preference for alignment. The vector sum of all the net moments in a given volume (V) results in a slight spin excess and gives a net magnetization vector (M),

$$M = \frac{1}{V} \sum \mu. \quad (\text{Eq. 2.2})$$

A conceptual example of the polarization of the magnetization vector can be seen in Fig. 2.1.

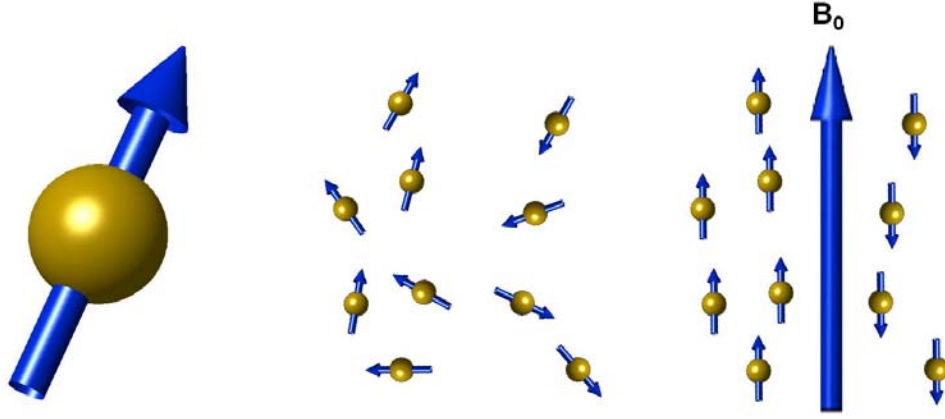


Fig 2.1: Polarization of the spins in MRI.

By convention the B_0 field is oriented in the longitudinal z -direction. In order to detect a signal, the equilibrium magnetization vector (M_0) is tipped away from the longitudinal axis by applying a radiofrequency (RF) field oriented orthogonal to the B_0 field for a short duration, creating a *RF pulse* known as B_1 . The B_1 field must be tuned to the Larmor frequency. The magnetization now has a transverse component (M_{xy}) which precesses around the B_0 axis at the Larmor frequency and a longitudinal component (M_z). M_{xy} has both magnitude and polar angle phase (ϕ) that give the position in the transverse xy -plane. The initial magnitude of the magnetization is determined by the angle (α), also known as the *flip angle*, by which the original longitudinal magnetization is tipped into the transverse plane and the initial phase (ϕ_0) is determined by the choice of rotational axis given by the RF pulse. While the transverse magnetization is precessing in the xy -plane, a MR signal can be measured via the inductive coupling between the magnetization vector and a receiver coil. The rotating magnetization induces a time-varying magnetic flux in the coil, which in turn induces a measureable time-varying voltage. A conceptual example of the generation and acquisition of the MR signal can be seen in Fig. 2.2.

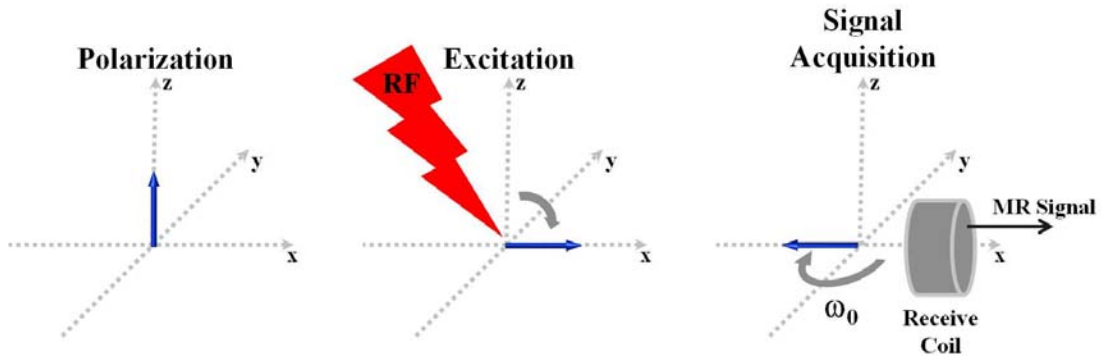


Fig 2.2: Acquisition of the MR Signal.

2.2.2 Intrinsic Contrast Mechanisms

The size of the equilibrium magnetization vector is directly proportional to the number of protons per unit volume, or the *spin density* (ρ_0). Hence, the spin density is a direct factor in the strength of the received MR signal. Two other factors in the MR signal strength are the T_1 and T_2 relaxations of the RF excited magnetization vector.

T_1 is known as the *spin-lattice* exponential decay or relaxation time constant for the regrowth of the magnetization vector along the longitudinal axis. Physically, T_1 involves the energy exchange between the nuclei and the surrounding lattice. T_1 relaxation is important because the magnitude of the recovering longitudinal magnetization directly limits the maximum magnetization that can be flipped into the transverse plan for generation the MR signal. Thermal equilibrium is restored when M_z regrows fully to M_0 . T_2 is known as the *spin-spin* exponential decay or relaxation time constant for the decay of transverse magnetization vector in the xy -plane. T_2 is dominated by the interactions between the dipole fields of individual spins. T_2 decay results from that de-coherence of the different spins and directly reduces the maximum signal available to generate the MR signal as time evolves following the RF excitation. For example, at a given time $t = TE$, the MR signal would be modulated by a factor e^{-TE/T_2} , the spin-spin decay factor. Furthermore, the MR signal typically suffers additional decay due to the dephasing of spins from external, static field inhomogeneities. This combined decay constant, known as T_2^* , is smaller than T_2 . These three tissue parameters (ρ_0 , T_1 , and T_2) provide the basis for intrinsic tissue contrast in MRI.

2.2.3 MR Image Formation

Linear gradients can be added to the system to generate a MR signal with spatially varying frequency components. The precession frequency of spins at a particular spatial location is now modified by a predetermined amount which allows the signal to be inverted with a Fourier transform to generate images in multiple dimensions. The ability to encode the image information in the spatial frequency domain, which is known as *k-space*, and to extract the image domain data with Fourier transforms is a powerful feature in MRI analyses. These spatially encoding gradients are typically known as i) a *frequency encode* or *readout* gradient and ii) a *phase encode* gradient in 2D. Phase encode gradients can also be extended to further dimensions. A conceptual example of this spatial encoding scheme can be seen in Fig. 2.3. In addition, a *slice select* gradient may be combined with the RF excitation pulse with a finite bandwidth to selective excite a layer or slice perpendicular to that gradient with a particular slice thickness. The addition of an offset to the center frequency of the RF pulse will shift the center location of the slice relative to the origin of the slice select axis.

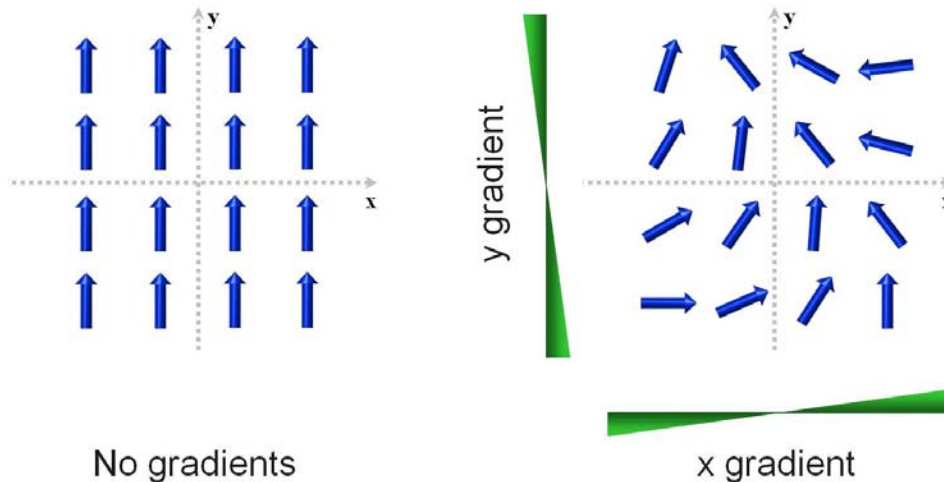


Fig 2.3: Spatial encoding with linear gradients for MR image formation.

The ability to play arbitrary waveforms on each of the linear gradient systems enables arbitrary slice select, readout, and phase encode gradients, which gives MRI a powerful and unique ability to generate arbitrary slice and volume orientations. Particular combinations and timings of RF pulses, gradient waveforms, and signal acquisitions (readouts) are known as a *pulse sequence*. In a pulse sequence diagram, the time between successive RF pulse excitations is typically known as the *repetition time* (TR) and the time when the dephasing of the spins has been partially refocused is known as the *echo time* (TE). For example in a *gradient recalled echo* (GRE) sequence, a fundamental pulse sequence in MRI, the spins are partially refocused causing a signal *echo* when the time integral of the readout gradient waveforms becomes zero. The signal acquisition by an analog to digital signal converter (ADC) is typically centered around TE . The pulse sequence diagram for the basic GRE sequence can be seen in Fig. 2.4.

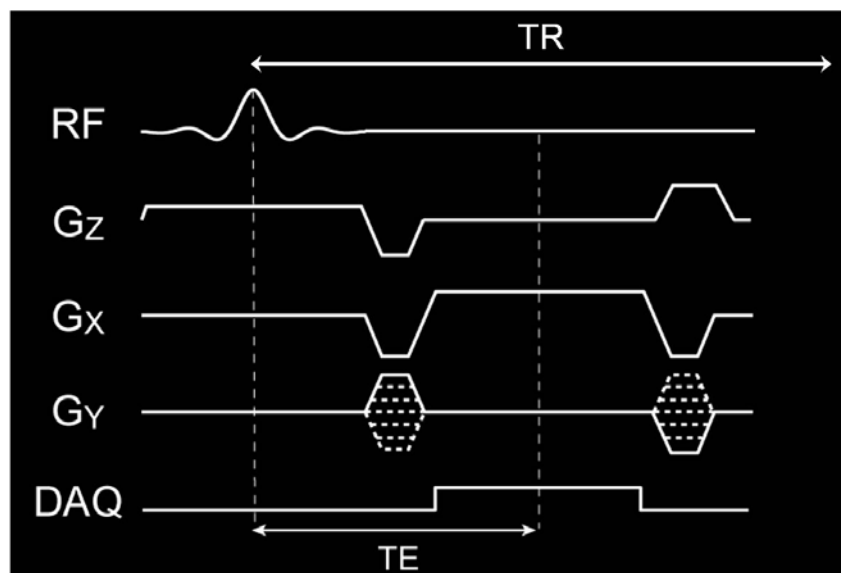


Fig 2.4: Gradient recalled echo (GRE) pulse sequence diagram.

2.3 Magnetic Susceptibility

Magnetic susceptibility is a quantitative proportionality constant that indicates a material's degree of magnetization in response to an applied magnetic field. If χ is negative, a material is classified as diamagnetic, which means the magnetization inside the material opposes the applied field and results in a net reduction of the applied magnetic field. Water and soft body tissues usually fall in the range of -7 to -11 ppm (9). On the other hand, if χ is positive, the magnetic field in the material is strengthened by the induced magnetization. Materials with positive χ are typically classified as paramagnetic, ferromagnetic, ferromagnetic, or antiferromagnetic. In general, materials that do not possess permanent magnetization without an external magnetic field are classified as diamagnetic or paramagnetic, depending on the sign, and have χ smaller in magnitude compared to the other types of magnetic materials.

MRI compatible materials are diamagnetic or weakly paramagnetic and these materials have bulk magnetic susceptibility on the scale of parts per million (ppm). However, the magnetic susceptibility plays a significant role in MRI and other MR applications since MRI has extremely stringent field homogeneity requirements. Most metal implants in the body are made of stainless steel, cobalt chrome, or titanium, with magnetic susceptibility weaker than 1000 ppm. These materials are safe in an MRI scanner but they can cause significant imaging artifacts, as discussed in Section 2.4. For the broader range of MRI-incompatible materials (e.g., ferromagnetic or anti-ferromagnetic materials) the bulk magnetic susceptibility is a critical consideration for the potential hazards of the magnetic forces and torques of materials brought into the B_0 field and is also common source of imaging artifacts. Magnetic susceptibility is also a source of endogenous MR contrast when susceptibility variations are found on a microscopic scale within tissues. For example, this might include blood flow, functional brain imaging, or diffusion imaging. In this thesis, magnetic susceptibility refers to volume magnetic susceptibility (instead of mass or molar susceptibility), is a dimensionless number in SI units, and is represented by the symbol, χ . Note that in some materials, such as many crystals, the magnetic susceptibility is not a scalar, depends on the orientation of the sample, and is defined as a tensor.

An object that is placed within an initially uniform magnetic field, such as the MRI B_0 field that is longitudinally oriented in the z -direction, becomes magnetized, induces its own field, and distorts the original field. The induced field within the material opposes the applied field. The induced magnetization varies spatially and is dependent on the sum of the applied and induced magnetic fields. A precise calculation of the magnetization and total field perturbation typically requires numerical methods, such as finite element modeling, to solve a partial differential equation boundary value problem. In addition to these numerical methods, Fourier transform-based methods have been developed recently to calculate field perturbations from arbitrary distributions of heterogeneous susceptibility distributions. However, the response of any ellipsoidal object with uniform χ placed in a uniform applied field can be calculated by algebraic methods. The solution for spheres and cylinders are special cases that can be used to quickly approximate a wide variety of other shapes. Table 2.1 lists the algebraic

solutions of the axial field perturbations, ΔB_z , for three commonly oriented shapes in a uniform B_0 MRI field. An example of the field gradients created by a simulated cylinder oriented perpendicular to the B_0 field is shown in Fig 2.5. The pattern of alternating positive and negative regions of field perturbations is commonly known as the *dipole effect* because a dipole with a similar orientation would generate the same field patterns.

	Inside the Object	Outside the Object
Long cylinder transverse to B_0 (radius a , axis along y -direction)	$\Delta B_z = \frac{\Delta\chi B_0}{2}$	$\Delta B_z = \frac{\Delta\chi B_0 a^2}{2} \frac{z^2 - x^2}{(x^2 + z^2)^2}$
Long cylinder parallel to B_0 (radius a , axis along z -direction)	$\Delta B_z = \Delta\chi B_0$	$\Delta B_z = 0$
Sphere (radius a) centered at origin	$\Delta B_z = \frac{2\Delta\chi B_0}{3}$	$\Delta B_z = \frac{\Delta\chi B_0 a^3}{3} \frac{2z^2 - x^2 - y^2}{(x^2 + y^2 + z^2)^{5/2}}$

Table 2.1: Field perturbation equations for common ellipsoid shapes with relative susceptibility $\Delta\chi$.

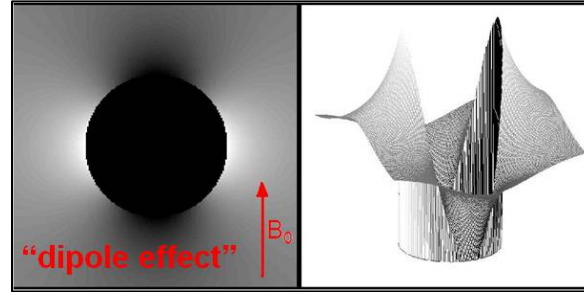


Fig 2.5: Simulation of ΔB_z for an infinitely long cylinder oriented perpendicular to the B_0 field.

2.4 Common Susceptibility Artifacts

As mentioned in Chapter 2.2, MRI uses a strong, static field (B_0) in the z -direction, an RF pulse (B_1) transverse to the z -direction, and three gradient fields (G_x , G_y , and G_z) to create images. The gradient fields are designed to have z -components which are linear in each orthogonal direction (x , y , and z). The gradients encode the precessing nuclear spins by altering the frequency and phase of the spins as a function of position. The resonance frequency of spins at each spatial location is proportional to the z -component of the field (B_z) at that location. Ideally this is

$$B_z(t) = B_0 + G_x(t)x + G_y(t)y + G_z(t)z. \quad (\text{Eq. 2.3})$$

Unfortunately, when a sample is placed into the uniform B_0 field, the heterogeneous distributions of magnetic susceptibilities create a static (time-independent) magnetic field perturbation that alters the z -component of the total field

$$B_z(t) = B_0 + G_x(t)x + G_y(t)y + G_z(t)z + \Delta B_z(x, y, z), \quad (\text{Eq. 2.4})$$

where $\Delta B_z(x, y, z)$, is the z -component of the field perturbations arising from the susceptibility regions and boundaries. $\Delta B_z(x, y, z)$ can be difficult to measure or predict and the effects on the MR images depend on its magnitude, orientation, and spatial extent relative to the gradients.

The off-resonance effects induced by field inhomogeneities lead to amplitude and phase dependent artifacts. These artifacts are also dependent on the spatial distribution of the inhomogeneities. Common artifacts induced by ΔB_z include intravoxel dephasing (signal dropout), blurring, voxels shifts, and image distortion. In terms of amplitude effects, the static field inhomogeneities lead to T_2^* decay, which may result in significant loss in the image signal if the signal is acquired too long after the RF excitation. Within an imaging voxel, this may directly lead to signal dropout. In addition, significant T_2^* decay during the readout period can cause a weighting (similar to a filter) in the k -space encoding trajectory, which corresponds to blurring in the image domain. Field inhomogeneities also introduce phase errors during the readout period, which cause deviations in the k -space encoding scheme. In essence, the change in phase caused by ΔB_z leads to errors in the spatial encoding mapping imposed by the linear gradients, which leads to incorrect voxel placement following reconstruction by Fourier analysis. These effects lead to voxels shifts and image distortion.

An example of a common distortion artifact is experimentally seen Fig. 2.6, where a cylinder (with relative susceptibility $\Delta\chi = 10$ ppm) oriented perpendicular to the B_0 field generates the dipole effect field perturbation pattern simulated in Fig 2.5. In the GRE images, the readout direction goes from left to right. During the frequency (readout) encoding process, the voxels near the two positive lobes are erroneously mapped to the left and the voxels near the two negative lobes are mapped to the right, causing the characteristic “bullet” or “spearhead” artifact in the readout direction.

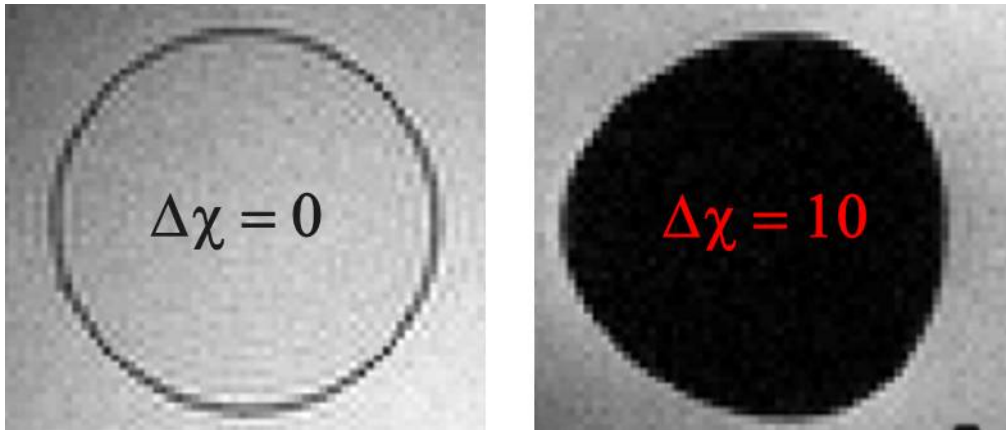


Fig 2.6: Image distortion in a GRE image due to $\Delta\chi = 10$ ppm. The common “bullet” or “spearhead” artifact in the readout direction.

Fig. 2.7 shows axial images of the brain from an echo planar imaging (EPI) and a reference GRE sequence. EPI is a common fast imaging technique that utilizes a relatively long readout time, which is particularly vulnerable to T_2^* effects. In the EPI image, signal dropout is particularly evident in the frontal and temporal lobes, which are near the sinus and aural air cavities. Blurring, image distortion, and voxel shifts are also evident across the slice. The high resolution GRE image is shown for reference.

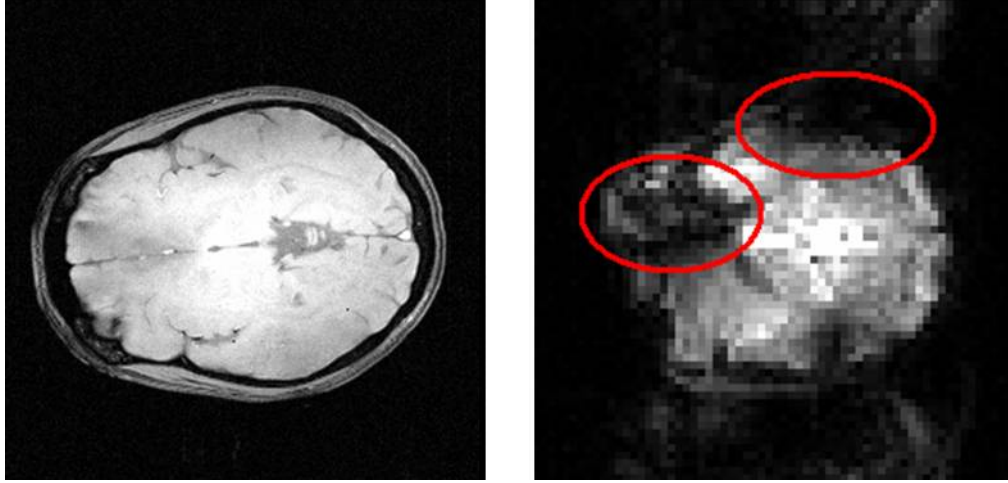


Fig 2.7: Signal dropout, blurring distortion in a 64x64 EPI image. EPI is a pulse sequence with a long readout time. High resolution 256x256 GRE images of the same axial brain slice shown for reference.

Hence the uniformity of the static field is critical in MRI. For example, the fundamental readout time is approximately $2T_2$. If T_2^* is significantly shorter than T_2 , then either SNR or resolution or both may be degraded. In order to achieve an example $T_2^* \sim T_2 = 50\text{ms}$, only $\sim 1/50$ ms off-resonance of ~ 20 Hz inhomogeneity *in a voxel* can be tolerated. 20 Hz is $\sim 1/3$ ppm at 1.5T (64 MHz) and it is $\sim 1/6$ ppm at 3 T (not accounting for change in T_2 due to increased field strength). This is an extremely difficult uniformity to achieve, and in practice ~ 1 ppm inhomogeneities can be tolerated for most applications.

2.5 B_0 Field Mapping

MRI-based B_0 field mapping is dependent on the complex (quadrature) detection of the MR signal, which gives angular phase (ϕ) information on the transverse magnetization generated by the application of a RF excitation field at the Larmor frequency (ω_0) to the aligned nuclear spins (10). Following excitation, the magnetization phase at the echo time (TE) is given by

$$\phi = \phi_0 + \omega TE, \quad (\text{Eq. 2.5})$$

where ϕ_0 is the initial phase given by the RF excitation and ω is related to the local static field perturbation (in a rotating reference frame of ω_0 with no chemical shift) by

$$\omega = \gamma \Delta B_z. \quad (\text{Eq. 2.6})$$

As before, ΔB_z is the field perturbation and γ is the gyromagnetic ratio, and Eq. 2.N becomes

$$\phi = \phi_0 + \gamma \Delta B_z TE. \quad (\text{Eq. 2.7})$$

Now consider two images acquired at two different echo times ($\Delta TE = TE_2 - TE_1$) with real and imaginary components related to their magnitudes and complex phase by Euler's formula: $IMG_1 = R_1 + iI_1 = M_1 e^{i\phi_1}$ and $IMG_2 = R_2 + iI_2 = M_2 e^{i\phi_2}$ with phases $\phi_1 = \phi_0 + \omega TE_1$ and $\phi_2 = \phi_0 + \omega TE_2$.

The phase difference of the two images is

$$\Delta\phi = \phi_2 - \phi_1 = \omega(TE_2 - TE_1) = \gamma \Delta B_0 \Delta TE. \quad (\text{Eq. 2.8})$$

Noting that

$$IMG_1^* \cdot IMG_2 = M_1 M_2 e^{i(\phi_2 - \phi_1)} = R_1 R_2 + I_1 I_2 + i(R_1 I_2 - I_1 R_2), \quad (\text{Eq. 2.9})$$

where IMG_1^* is the complex conjugate of IMG_1 and the phase difference is also equal to

$$\Delta\phi = \phi_2 - \phi_1 = \arg(IMG_1^* \cdot IMG_2), \quad (\text{Eq. 2.10})$$

then the magnetic field variation is easily computed by

$$\Delta B_z = \frac{\Delta\phi}{\gamma \Delta TE}, \quad (\text{Eq. 2.11})$$

where the phase difference is now also given by

$$\Delta\phi = \tan^{-1} \left(\frac{R_1 I_2 - I_1 R_2}{R_1 R_2 + I_1 I_2} \right). \quad (\text{Eq. 2.12})$$

Phase differences which are greater than $\pm\pi$ must be unwrapped due to the periodic nature of the tangent function. Fig 2.8 shows an example of wrapped and unwrapped field maps. Existing phase unwrapping algorithms fall into either spatial or temporal categories. An example of the spatial technique is the Phase Region Expanding Labeler for Unwrapping Discrete Estimates (PRELUDE), which optimizes a cost function that identifies neighborhoods of unwrapped phases and iteratively merges the regions until a single unwrapped region remains (11). The temporal approach typically acquires several sets of images with increasingly longer TE . The initial field map with minimum TE is assumed to be unwrapped (by choosing a small ΔTE), and successive field maps with increasing ΔTE can have values of $\pm 2\pi$ added until it falls within the unwrapped regime. As each new field map is computed, the trend can provide a better estimate of the slope and improve the field map with each additional image set (10).

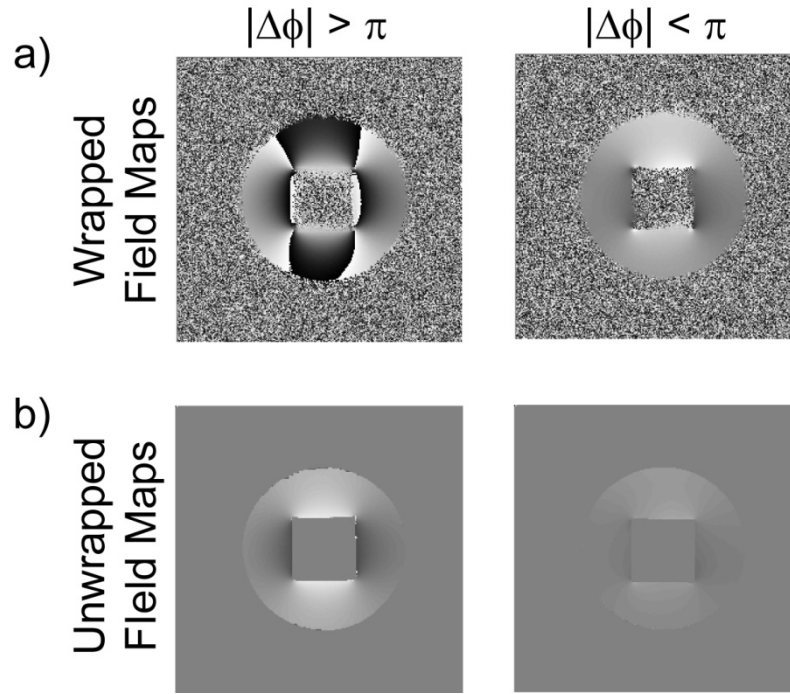


Fig 2.8: Wrapped and Unwrapped field maps for the cases of phase differences ($\Delta\phi$) greater or less than π . The unwrapped field maps are also masked to remove the noise from the regions with no signal.

Chapter 3

Pyrolytic Graphite Foam Magnetic Susceptibility Matching Theory

3.1 Introduction

The B_0 field is typically statically shimmed to be uniform to a few ppm across a large FOV, typically 50 cm DSV. Unfortunately, magnetic susceptibility boundaries introduced by a sample or body placed into the magnet bore gives rise to steep field perturbations over a few centimeters, which can be as high as ± 5 ppm at air and tissue boundaries, for example. These higher spatial frequency field gradients can often be difficult to dynamically shim away to homogenize the static field.

A simple method to minimize some of these field inhomogeneities is simply to eliminate the boundaries. For example, the field gradients in a particular region of interest (ROI) in the body arising from an external air cavity may be mitigated by filling the cavity with a material with the same magnetic susceptibility, effectively eliminating the interface. Other areas of the body may be wrapped with a tissue susceptibility matching material, which has the effect of moving the interfaces and the corresponding field perturbations away from the ROI to the new air and material interface. This is known as passive susceptibility matching. A conceptual example of this is shown in Fig 3.1.

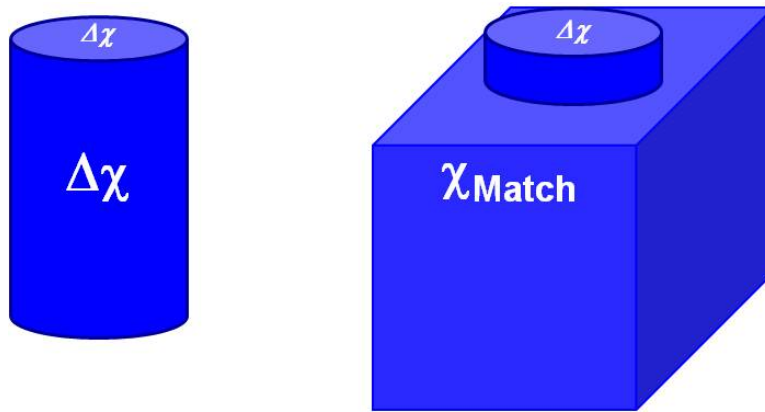


Fig 3.1: Passive susceptibility matching concept diagram.

In this chapter, the theory behind a composite passive tissue susceptibility matched foam is developed. Highly anisotropic pyrolytic graphite (PG) particles are randomly dispersed into polyurethane foams at a specific volume fraction to create a bulk isotropic magnetic susceptibility matching material. Conductivity, Q , and RF power deposition concepts are reviewed to ensure that PG foams will not reduce SNR or cause patient heating.

3.2 Pyrolytic Graphite

Pyrolytic graphite (PG) is a polycrystalline form of carbon that has a hexagonal crystal structure, much like normal graphite (12). It crystallizes in a planar order resulting in stacks of graphene sheets, which produces a single cleavage plane. Due to these highly ordered layers, pyrolytic graphite has well-known anisotropic properties (13). For example, it is on the order of 10^4 times more electrically conductive parallel to its crystal plane than perpendicular to the plane (14). Pyrolytic graphite also has anisotropic diamagnetic susceptibility that is 70 times greater perpendicular to its crystal plane ($\chi_{\perp} = -595$ ppm) than parallel to the plane ($\chi_{\parallel} = -8.5$ ppm) (9). The susceptibility anisotropy of the PG crystal is illustrated in Fig 3.2.

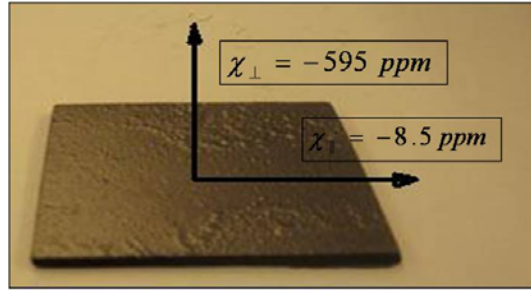


Fig 3.2: Pyrolytic graphite crystals exhibit anisotropic magnetic susceptibility.

3.3 Composite Bulk Magnetic Susceptibility

We take advantage of the anisotropic diamagnetic susceptibility of pyrolytic graphite to create an isotropic, two-phase composite material consisting of diamagnetic pyrolytic graphite particles embedded in dielectric matrices useful for tissue magnetic susceptibility matching. We have calculated that we can control the isotropic susceptibility of a material by embedding a small volume fraction of randomly oriented powdered pyrolytic graphite particles into a closed-cell polyurethane foam.

We first calculate the effect of randomly dispersing PG particles into the foam. The average susceptibility of a dispersion of small magnetic particles in a less magnetic matrix can be estimated in terms of the volume fraction f of the magnetic particles (9):

$$\sigma_{PG} = \frac{f\chi}{1+\alpha\chi}, \quad (\text{Eq. 3.1})$$

where σ_{PG} is the overall magnetic susceptibility of the dispersed particles and α is a shape dependent demagnetizing factor between 0 and 1. Because χ is on the order of part per million, the denominator of Eq. 3.1 approaches unity and the total equation reduces to

$$\chi_{avg} = f\chi. \quad (\text{Eq. 3.2})$$

Note that this implies that the shapes of the crystal (sphere versus rod or rhombus) have negligible effect on the bulk magnetic susceptibility of the composite, which greatly simplifies the design of the composite.

The magnetic susceptibility of the PG foam has contributions from a volume fraction f of the uniformly dispersed and randomly oriented PG, which has a magnetic susceptibility (χ_{Total}) equivalent to the average of its directional components χ_1 , χ_2 , and χ_3 (15,16),

$$\chi_{Total} = \frac{(\chi_1 + \chi_2 + \chi_3)}{3} = \frac{(\chi_{\perp} + 2\chi_{\parallel})}{3}, \quad (\text{Eq. 3.3})$$

and from the remaining volume fraction $(1 - f)$ of the foam, which has the equivalent susceptibility of air ($\chi_{Air} = 0.36$ ppm) and is equal to

$$\chi_{PG \text{ Foam}} = \chi_{Total}f + \chi_{Air}(1 - f). \quad (\text{Eq. 3.4})$$

Thus, the equation for the magnetic susceptibility of the pyrolytic graphite foam ($\chi_{PG \text{ Foam}}$) is

$$\chi_{PG \text{ Foam}} = -204.4f + 0.36 \text{ ppm}, \quad (\text{Eq. 3.5})$$

where f is the volume fraction of the pyrolytic graphite foam. Eq. 3.5 predicts a pyrolytic graphite volume fraction $f \sim 0.045$ to match human tissue susceptibility of ~ -9 ppm (9). Note that 10% error in the ideal volume fraction translates to susceptibility values between -8.5 to -9.5 ppm, or within 1 ppm of human tissue susceptibility. This tolerance is generous, which is encouraging for the robustness of the susceptibility matching under variable compression of the PG foam. To prevent significant compression, we rely on closed-cell foams. Fig 3.3 shows a conceptual diagram on the use of a PG foam cushion.

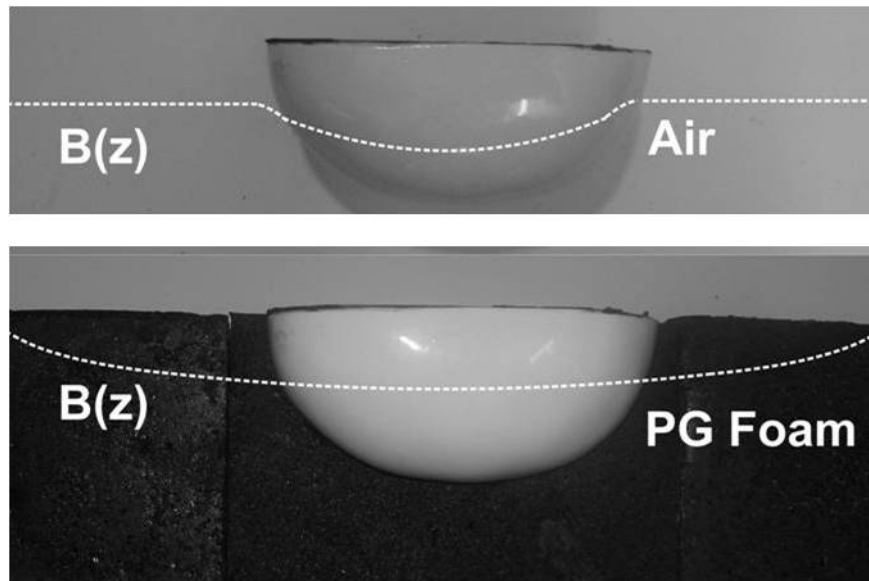


Fig 3.3: Conceptual diagram of passive tissue susceptibility matching PG foam.

3.4 Composite Electrical Conductivity

As with all materials to be used with patients in MRI, we are concerned not only with its magnetic susceptibility and effects on the main field, but also its MRI compatibility. In particular, we must avoid using a conductive material, which could burn the patient. Conductive materials support eddy currents which cause heating, which could ultimately lead to patient discomfort or even injury. Also we would not want the PG foam to add a significant amount of noise to the MRI scan. MRI noise scales linearly with the conductivity of the sample and quadratically with the radius (17). Because the foam will be packed around the patient, it is important for the conductivity of the pyrolytic graphite foam to be at least two orders of magnitude below that of human tissue, which is approximately 0.5-1.0 S/m (18). Hence the electrical conductivity should ideally be below 5 mS/m so that the noise contribution from the PG foam will be negligible. This was a significant concern given the very high conductivity (in plane) of the individual PG crystals ($\sigma_{PG} = 1.9 \times 10^6$ [S/m]) (14). Fortunately, at the 4.5% volume concentration used here for human tissue matching, the PG crystals are largely insulated from each other, rendering the bulk conductivity to be nearly identical to the conductivity of the foam. This is explained below using the “effective medium theories (EMTs)”, which are commonly used to model and predict the electromagnetic properties of two phase conductor/insulator composites.

EMTs include the Maxwell and the symmetric media Bruggeman formulas to predict the conductivity σ_{em} of effective media. These media have a highly conducting component with conductivity σ_h and an insulating component with conductivity σ_l . The simplest effective media equations for dilute solutions of spherical inclusions ($f_h \leq 0.1$), the Maxwell equations (19,20), predict

$$\sigma_{em} = \frac{\sigma_l}{1-3f_h}, \quad (\text{Eq. 3.6})$$

when $\sigma_h \rightarrow \infty$ and where f_h is the volume fraction of the conducting component. Applied to the PG foam ($f_h \sim 0.045$), Eq. 3.6 suggests that the conductivity of the PG foam will approach that of the insulating foam.

The EMTs also suggest that the insulating components coat and insulate the conducting inclusions and prevent the formation of conduction paths within the composite material. As the concentration of inclusions increase, they begin to touch and form conduction paths, increasing the conductivity. Because the limiting conditions for the Maxwell equations are not met ($\sigma_h \neq \infty$), we introduce the symmetric Bruggeman equation to evaluate the conductivity of our PG foams for general conditions.

The Bruggeman equation predicts a relationship between σ_{em} and the known quantities,

$$f_l \frac{\sigma_l - \sigma_{em}}{\sigma_l + 2\sigma_{em}} + f_h \frac{\sigma_h - \sigma_{em}}{\sigma_h + 2\sigma_{em}} = 0, \quad (\text{Eq. 3.7})$$

for spherical inclusions of high conductivity in a low conductivity matrix (20). Eq. 3.7 reduces to the Maxwell equations under the previous conditions in the dilute limit, as expected. Under our conditions for pyrolytic graphite foam with volume fraction $f = 0.045$, $\sigma_{PG} = 1.9 \times 10^6$ S/m, and $\sigma_{Foam} = 10^{-4}$ S/m (21), solving for σ_{em} in Eq. 3.7 yields a solution $\sigma_{em} = 1.1 \times 10^{-4}$ S/m. In addition, increasing χ_{Foam} up to 1 S/m to simulate far more conductive foams yields solutions of $\sigma_{em} \sim 1.1 \sigma_{Foam}$. Thus, the solutions of σ_{em} are on the same order of magnitude as χ_{Foam} . Consequently, we expect that the composite pyrolytic graphite foam is approximately 3 orders of magnitude lower in conductivity than human tissue.

Eq. 3.7 holds for solutions below the vicinity of the percolation threshold, the point where the crystals begin to touch and to form conduction paths. However, calculations indicate that the crystals will not form significant conduction paths until the volume fraction of PG crystals is approximately 16% (19), which is approximately 3-4 times higher than the volume fraction required for human tissue susceptibility matching with PG foam. More complicated EMTs, such as the General Bruggeman formula, include parameters to account for percolation (19,20,22), but are not necessary for our desired concentration of particles. This theory would be important, however, if long rods, e.g. carbon nanotubes, were used instead of spherical particles. We believe that roughly spherical crystals are the best option since they minimize the chances of particles forming conduction loops.

3.5 Quality Factor

The quality factor or Q factor of an oscillator or a resonator is a dimensionless parameter that characterizes how under-damped it is. A higher Q indicates that a lower rate of energy is lost relative to the stored energy during each oscillation, so a higher Q oscillator would “ring” longer before being fully damped. For a resonant MRI coil, Q is defined as

$$Q = \frac{\text{peak magnetic energy stored}}{\text{average energy dissipated per cycle}}, \quad (\text{Eq 3.8})$$

at the resonant frequency ω_0 . Equivalently, Q can be defined as

$$Q = \omega_0 \frac{L}{R_{coil}}, \quad (\text{Eq 3.9})$$

where L is the reactive impedance and R_{coil} is the resistive impedance. Q can be measured by computing the ratio

$$Q = \frac{\omega_0}{2\Delta\omega}, \quad (\text{Eq 3.10})$$

where $2\Delta\omega$ is the full width at half maximum (FWHM) around the resonant peak of the resistance (23).

In MRI, the receiver coil is inductively coupled to the test sample to acquire the MR signal from the rotating magnetization. Conductive losses in the sample result in coil loading, which in turn results in a reduction in coil Q . In addition, any currents that flow in a sample will add noise to the receiver coil, which lower the SNR. Thus, it is paramount that a passive susceptibility matching material such as PG foam be nonconductive so that the extra sample volume used for susceptibility matching does not further load the coil or add noise to the MR signal. Here we expect that the conducting PG particles will be insulated from forming conduction loops in the foam composite matrix, which will result in no loss of Q from using PG foams in the receiver coil. The SNR of an image acquired with the addition of PG foam should also not decrease. In regions where T_2^* -induced intravoxel dephasing occurs, the addition of PG foam has the possibility of increasing SNR by removing the loss of signal artifacts.

3.6 RF Power Deposition

RF magnetic field pulses are used to manipulate the macroscopic magnetization vectors in MRI and its related applications. Tissue heating is thus a potential safety concern because some portion of the transmitted RF energy may be absorbed by the body. Thus it is important for patient safety to limit whole body and localized heating to appropriate levels (24-26). Typically whole body heating is limited to prevent the elevation of core body temperatures to potentially life threatening levels. For local RF excitations, caution is taken to prevent localized burns on the patient. RF power deposition is typically measured by the specific absorption rate (SAR), which is formally defined as the time derivative of the incremental energy absorbed by an incremental mass contained in a volume of a given density (27).

The SAR from the RF field can be estimated from quasistatic analysis. For example, consider a sphere of radius R and conductivity σ excited by a uniform RF excitation pulse B at a frequency ω . According to Faraday's law, the electric field \mathbf{E} vector is related to the time rate of change of flux density vector \mathbf{B} by

$$\oint \mathbf{E} \cdot d\mathbf{l} = \frac{d}{dt} \iint \mathbf{B} \cdot d\mathbf{s}, \quad (\text{Eq. 3.11})$$

Since \mathbf{B} is uniform over the region of path radius R , the scalar strength of the electric field E is given by

$$E = \frac{R}{2} \frac{dB}{dt}, \quad (\text{Eq. 3.12}).$$

where B is the peak magnetic field strength. Because the magnetic field varies sinusoidally as

$$B = B_1 \sin \omega t, \quad (\text{Eq. 3.13})$$

Eq. 3.12 becomes

$$E = \frac{R}{2} \omega B_1 \cos \omega t. \quad (\text{Eq. 3.14})$$

Combined with the power density

$$\frac{dP}{dV} = \frac{\sigma E^2}{2}, \quad (\text{Eq. 3.15})$$

and integrated over the volume of the sphere, the total RF power deposited (P_{total}) is given by

$$P_{total} = \frac{\sigma \pi \omega^2 B_1^2 R^5}{15}. \quad (\text{Eq. 3.16})$$

The average specific absorption rate (SAR_{avg}) with duty cycle D and tissue density ρ simplifies to

$$SAR_{avg} = \frac{P_{total}}{\rho \left(\frac{4}{3} \pi R^3 \right)} = \frac{\sigma D \omega^2 B_1^2 R^5}{20 \rho}, \quad (\text{Eq. 3.17})$$

where SAR_{avg} is typically expressed in units of W/kg. Therefore, the conductivity of a susceptibility matching material such as PG foam must be minimized to limit SAR.

Chapter 4

Pyrolytic Graphite Foam Proof of Concept and Safety Testing

4.1 Introduction

In MR studies, the uniformity of the B_0 main field is critical for image signal and contrast. In particular, the 9 ppm magnetic susceptibility difference between air and tissue produces magnetic field perturbations near the skin and near the lungs. These are known to cause significant MRI artifacts including unreliable fat suppression, intravoxel dephasing, blurring, and voxel shifts. Certain pulse techniques, such as echo planar imaging (EPI), balanced steady state free precession (bSSFP), blood oxygen level dependent (BOLD) contrast, gradient recalled echo imaging (GRE) and fat suppression methods suffer particularly from B_0 field inhomogeneities (9,28). Furthermore, the absolute size of the perturbations also increases as the strength of the B_0 field increases, making artifact-free imaging at 3.0 T and above a challenge. Susceptibility artifacts make it more difficult to conduct robust MR studies for any applications that require exceptionally uniform B_0 fields, such as fat suppression, BOLD fMRI (29), extremity MRI, and spectroscopy (30).

Susceptibility artifacts can be reduced by directly compensating for the B_0 inhomogeneities with either active or passive methods. Actively shimming the region of interest (ROI) with gradient shims and low order spherical harmonic shim coils is common in MRI studies. However, active and dynamic shim methods cannot correct for high spatial frequency perturbations (31-33), since the shim coils must be large to admit the patient. Large coils cannot generate high spatial frequency field patterns deep within a patient (9). However, these high spatial frequency perturbations are invariably present near abrupt skin-tissue interfaces, such as those found near the breast, shoulders, chin, and extremities. Other types of shims include diamagnetic crystal pyrolytic graphite (PG) shims (34-36) that have been placed in the subject's mouth to shim the field within the brain. Here the small, solid PG shims are shaped to partially compensate for field inhomogeneity induced by air within the sinuses. A similar, active shim method using localized external current carrying coils has also been developed to compensate for inhomogeneities in the human prefrontal cortex (37,38). These sets of well-defined shim coils were designed and tailored specifically for the local field distortions caused by the multi-air cavity system of the sinuses, and were located outside the patient.

A popular method to improve field homogeneity near the skin is to cover the skin with a tissue susceptibility matched material to move the inhomogeneities outside the field of view or ROI. This is a simple, passive, and direct technique for reducing B_0 inhomogeneities at air and tissue boundaries. Previous versions of these techniques include bags of fluid, such as perfluorocarbon (39), barium sulfate doped water (40),

Kaopectate (41), or other MRI invisible agents. However, it can be difficult to shape a fluid to conform to the body, and these fluids are typically incompatible with an embedded RF coil. In addition, these materials have specific densities close to one, and hence can be quite heavy when of adequate size.

Previous finite element simulations by Bhagwendian on simple geometries such as spheres and cylinders suggest that increasing the size of the object can shift the high frequency perturbations at the interface outside the original ROI (42). This suggests that surrounding a target region with a layer of susceptibility matched material would result in a more homogenous field near the tissue/material interface and is depicted in Fig. 4.1. The necessary size of this matching layer, which is approximately a radius for cylinders and spheres, suggests a lower density material is preferable. For example, surrounding a patient head with a 3 in. shell of tissue susceptibility matched material in a typical head coil can improve homogeneity near the skin interface.

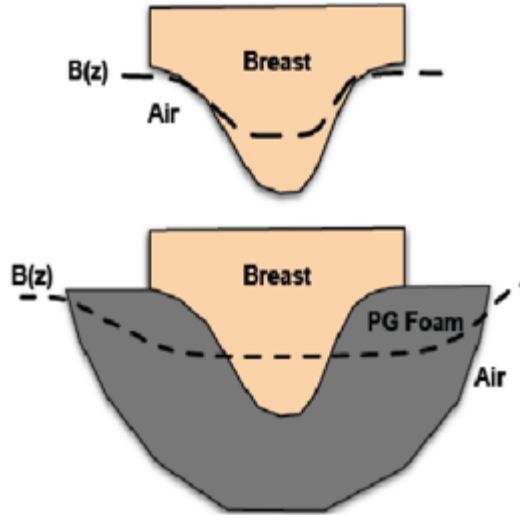


Fig 4.1: Concept illustration of magnetic field homogeneity in the breast. Field perturbations are present near the air/tissue interface without PG foam (**top**). By surrounding the skin with tissue susceptibility matched PG foam (**bottom**), the perturbations are shifted further away from the skin and the magnetic field is more uniform inside the breast. This pristine field homogeneity would allow for more efficient fat suppression, which is critical for the early detection of breast tumors.

In this chapter we present a new passive method to reduce field perturbations and to achieve improved B_0 homogeneity near the skin. Here, instead of a fluid, we employ a lightweight, composite closed cell foam. The key innovation was to dope the closed-cell foam with a randomized, uniform dispersion of pyrolytic graphite (PG) microparticles to match the magnetic susceptibility of human tissue. Hence, the lightweight PG foam composite may become a convenient alternative to the fluid matching agents discussed above for moving the high spatial frequency perturbations outside the tissue of interest. Unlike fluid susceptibility matching agents, the PG foam is simple to shape, lightweight, and can be embedded directly within an RF coil. Because foam padding is ubiquitous in the MR suite, PG foam can be easily adapted for use for a wide variety of applications,

such as spectroscopy, patient studies, especially for extremity MRI, and small animal imaging.

In this chapter, we show experimentally that the PG foam composite matches the magnetic susceptibility of water. We calculate a tolerance of at least 10% in targeted PG volume fraction for improved susceptibility matching. We demonstrate the PG foam reduces susceptibility induced artifacts in EPI images. We also show that the foam is three orders of magnitude less conductive than human tissue, so it is safe to use in an MRI scanner and it will add virtually no noise to the scan. We also demonstrate that PG foam is lightweight and produces no MRI signal.

4.2 Methods

4.2.1 PG Foam Construction

Pyrolytic graphite (PG) foams were created by dispersing high purity PG powder (Asbury Carbons, Asbury NJ) into a closed-cell, two-component polyurethane polymer foam (Silpak, Inc., Pomona, CA). PG particles were ~44 microns in median diameter. PG powder was uniformly dispersed into one component of the foam prior to mixing both foam components. The foam was then poured in plastic containers of various sizes or custom built plastic molds and allowed to rise and cure. We targeted PG foams with volume fraction $f = 0.045$ to match human tissue susceptibility of -9 ppm, based on our theoretical calculations (see Section 3.3) for base foam with $\chi_{Foam} = \chi_{Air} = 0.36$ ppm. Foams of $f = 0$ to 0.05 (0-5%) in 0.005 (0.5%) increments were also made for testing purposes. PG volume fraction was controlled by dispersing a calculated mass of PG based on density calculations relative to final targeted foam volume.

4.2.2 Phantom MRI Field Maps

Test phantoms were built to observe and quantify field gradients near susceptibility interfaces. A proof of concept phantom was constructed with three (1.5 in. diameter) plastic cylinders (United States Plastics Corp., Lima, OH) oriented orthogonal to the main B_0 field and immersed in a sealed, larger cylinder filled with $MnCl_2$ doped water. The water was doped to simulate tissue relaxation times (43). The smaller cylinders were filled with doped water, air, and PG foam, respectively, to create the relevant susceptibility boundaries. Tissue susceptibility matched PG foam ($f = 0.045$ for base foam with $\chi_{Foam} = \chi_{Air} = 0.36$ ppm) was used in the phantom. Similar plastic cylinders containing other volume fractions of PG foam were also created for testing purposes and individually immersed in doped water.

For the proof of concept phantom, coronal high spatial resolution, 2D multislice gradient echo images were acquired for magnitude and off-resonance field maps on a 3T whole body Siemens Trio (Siemens Medical Solutions, Malvern, PA) scanner equipped with a standard 12 channel head coil. The field of view of the 256 x 256 magnitude images was 22.4 x 22.4 cm² in-plane (0.875 x 0.875 mm² spatial resolution) with 4 mm slice thickness. TR/TE of the gradient echo images was 261.9/5 ms. A series of two

similar 3D gradient echo scans with the same FOV were acquired to compute off-resonance field maps. TR of both scans was 488 ms. TE was 4.92 and 7.38 ms for the two scans, respectively. Off resonance field maps were computed using the phase accrual data between the two sets of gradient echo images by dividing phase maps by ΔTE (44) using custom in-house code. This field map reconstruction did not include a phase unwrapping algorithm in order to produce a qualitative view of the extent of the phase wrapping caused by the field inhomogeneities.

A second series of field maps were acquired on a 3T GE Signa scanner (General Electric, Waukesha, WI, USA) using a custom GE IDEAL (Iterative Decomposition of water/fat using Echo Asymmetry and Least-squares estimation) pulse sequence on the various volume fractions of PG foam. The FOV of the 256 x 256 field maps was again 22.4 x 22.4 cm² in-plane (0.875 x 0.875 mm² spatial resolution) with 4 mm slice thickness. The TR of the IDEAL sequence was set at 6.3 ms, and utilized various TE (base TE = 2 ms). Field maps were auto-computed using the IDEAL sequence data and a built-in iterative reconstruction algorithm. These field maps included a phase unwrapping algorithm in order to produce quantitative view of the field inhomogeneities.

4.2.3 Echo Planar Imaging with PG Foam

Custom phantom test apparatuses were built to quantify field gradients near the susceptibility interfaces. Sets of two-compartment plastic apparatuses were constructed using a rectangular container (58 x 58 x 150 mm³) mounted inside of a larger cylindrical container (152 mm diameter, height). The containers were oriented orthogonal to the B_0 field. The surrounding cylindrical compartments were filled with MnCl₂-doped water to create a region with tissue-like susceptibility in the phantom. The smaller rectangular containers were filled with air, MnCl₂-doped water, or susceptibility matching PG foam blocks (N = 4) to create the relevant susceptibility boundaries.

3T field maps were acquired on a Siemens scanner with a standard head coil as before (Section 4.2.2). The field of view of the 256 x 256 field maps was 25.6 x 25.6 cm² in-plane (1.0 x 1.0 mm² spatial resolution) with 3 mm slice thickness. Coronal 3D multi-slice echo planar images (EPI) of the phantoms were acquired to observe the effects of the susceptibility induced field inhomogeneities on a long readout time pulse sequence. The FOV and slice thickness of the 64 x 64 images (4.0 x 4.0 mm² spatial resolution) were the same as the field maps. TR/TE of the EPI sequence was 2000/28 ms.

4.2.4 PG Foam Safety and RF Compatibility Testing

Q measurements of the PG foams, with f from 0.5 to 5%, along with regular foam, PG powder, and human heads were measured with an HP 4195A 1-500 MHz spectrum analyzer (Agilent Technologies, Palo Alto, CA) and a tuned 4T MR head coil using a transmission method described previously (45) with N = 6 samples each to compare conductivities. Foam samples were approximately 4.5 L in volume to simulate a tissue volume larger than the average human head.

PG foam heating was investigated by placing foams in a 3T Siemens Trio (Siemens Medical Solutions, Malvern, PA) scanner equipped with a standard 12 channel head coil during two SAR intensive pulse sequences, including fast spin echo ($\alpha = 180^\circ$) and bSSFP ($\alpha = 70^\circ$), for 10 minutes. Sequence parameters were chosen to reach the SAR limits of the system for each sequence. Changes in foam temperature were measured with a Luxtron m3300 optical probe (Lumisense Technologies, Santa Clara, CA).

4.2.5 PG Foam Modifications

Custom Plasticizer

Sets of PG foams blocks ($N = 4$) of various $f = 0$ to 0.055 (0-5.5%) were made as before (Section 4.2.1) with the addition of a custom plasticizer (Silpak, Inc., Pomona, CA) to reduce the viscosity of the initial foam slurry to facilitate homogeneous mixing and to create softer foams for patient comfort. The plasticizer was also slightly diamagnetic ($\chi_{\text{plasticizer}} \sim -1$ ppm), which reduced the target volume fraction from $f = 0.045$ to $f = 0.039$. 3T field maps of air, water, and PG foam phantoms were acquired on a Siemens scanner with a standard head coil as before (Section 4.2.3). The field of view of the 256 x 256 field maps was 25.6 x 25.6 cm² in-plane (1.0 x 1.0 mm² spatial resolution) with 3 mm slice thickness.

Larger PG Particles

Sets of PG foams blocks ($N = 4$) of various $f = 0$ to 0.053 (0-5.3%) were made with the addition of the custom plasticizer as before with the replacement of the 44 micron particles with 100 micron particles (Asbury Carbons, Asbury NJ) to further reduce the viscosity of the initial foam slurry. Both sets of PG particles were imaged with a microscope (Model AE31, Motic Group, British Columbia, Canada) for qualitative comparison purposes. The target volume fraction with the use of the plasticizer and the larger particles was $f = 0.039$ as before. 3T field maps of air, water, and PG foam phantoms were acquired on a Siemens scanner with a standard head coil as before (Section 4.2.3) to verify that the increase in particle size would have no effect of the target volume fraction for susceptibility matching. The field of view of the 256 x 256 field maps was 25.6 x 25.6 cm² in-plane (1.0 x 1.0 mm² spatial resolution) with 3 mm slice thickness. The standard deviation (σ) of the field perturbations for each phantom was computed as a measure of dispersion.

4.3 Results

4.3.1 PG Foam and MRI Phantom Images

Figure 4.2a shows a large PG foam sample (10 in. diameter, 3.5 in. height) of $f = 3\%$. The foam has a final density of 0.2 g/mL. Figures 4.2b and 4.2c show other foam shapes of similar density with $f = 4.5\%$ created for testing use or for padding purposes. Figure 4.3 shows the magnitude image (a) and off-resonance field map (b) of the proof of

concept phantom. In the magnitude image, there is no signal from the PG foam and air cylinders as expected in the magnitude image. There is also significant geometric distortion in the air cylinder portion of the phantom. In the off-resonance field map, the air/water interface causes the classic dipole field pattern outside the air-filled cylinder. The field maps also show that the PG foam demonstrates susceptibility matching to the doped water.

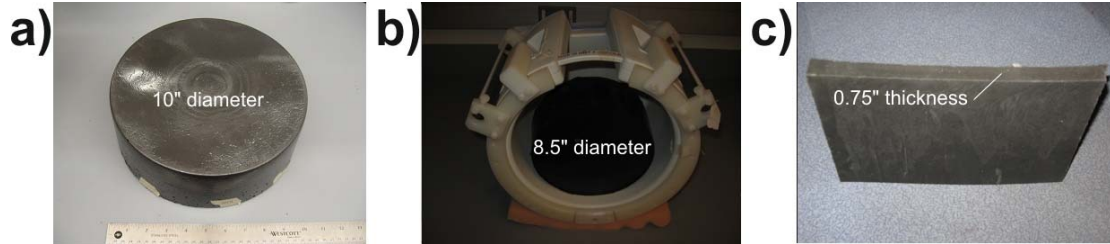


Fig 4.2: Examples of tissue susceptibility matched PG foam. a) A large PG foam sample (10 in. diameter). b) A 4.5 L sample (8.5 in diameter) PG foam in a Varian 4T head coil. This setup was used for conductivity and heating tests. c) An example of 0.75 in. thick sheets of PG foam that can be used for padding or wrapping patients in an MRI exam.

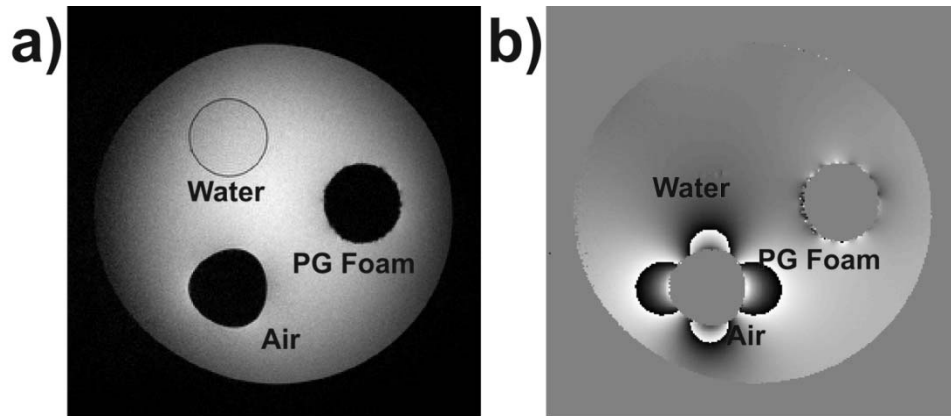


Fig 4.3: Example of water susceptibility matching using PG foam. a) A 3T coronal image of a PG foam, air, and water phantom acquired with a gradient echo sequence, TR/TE = 200/5 ms, slice thickness = 4 mm, FOV = 22.4 x 22.4 cm², matrix = 256x256. Significant distortion is seen near the air cylinder. b) B₀ field map of the phantom. The classic ± 5 ppm dipole effect is seen outside of the air cylinder but is significantly reduced outside the PG foam indicating improved susceptibility matching.

Figure 4.4 shows individual field maps of (a) water, (b) air, (c) regular foam, (d) $f = 1.5\%$ PG foam, (e) $f = 4\%$ PG foam, and (f) $f = 4.5\%$ PG foam immersed in doped water. Figures 4.4b and 2.4c indicate that the regular foam shows a dipole pattern similar in magnitude to the pattern resulting from air indicating equivalent magnetic susceptibility. The poorly matched PG foam ($f = 1.5\%$) in Figure 4.4d shows a reduced dipole pattern, but still results in substantial field perturbations. The water matched PG foam ($f = 4.5\%$) in Figure 4.4f demonstrates 5-10x reduction in off-resonance effects depending on location as compared to the air, suggesting field homogeneity within ± 1 ppm outside the PG foam cylinder as compared to ± 5 ppm near the air cylinder. In addition, the predicted $\sim 10\%$ deviation from the targeted $f = 4.5\%$ volume fraction is apparent in the significantly reduced dipole pattern found in Figure 4.4e.

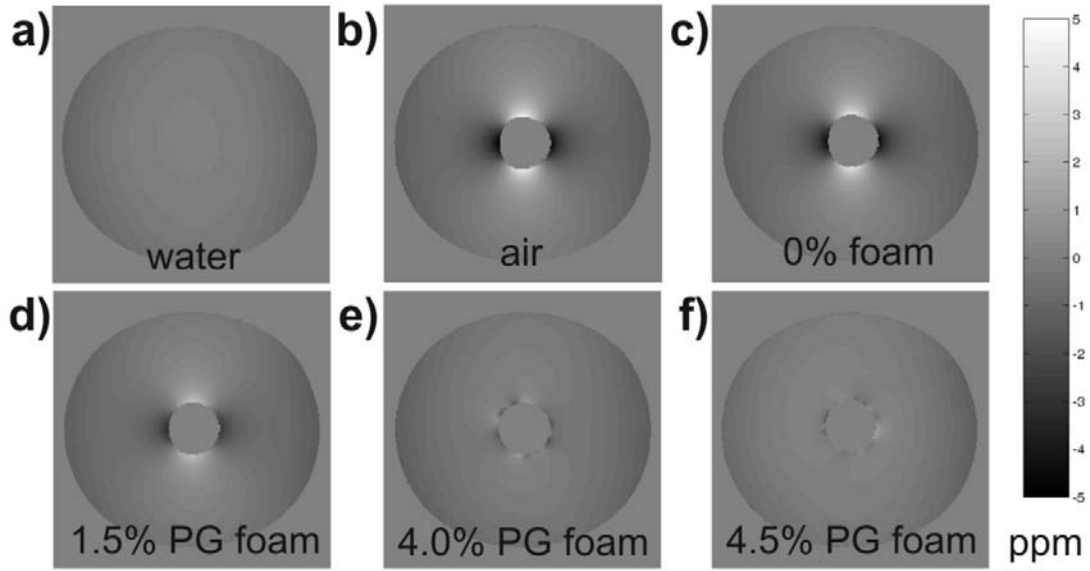


Fig 4.4: B_0 field maps of individual water, air and PG foam phantoms. 3T coronal field maps were acquired with a custom GE IDEAL pulse sequence with a built in iterative reconstruction algorithm, TR= 6.3 with variable TE, slice thickness = 4 mm, FOV = 22.4 x 22.4 cm², matrix = 256x256. a) Perfect susceptibility matching is shown with water. b)-c) Air and regular foam each shows the classic ± 5 ppm dipole effect indicating equivalent magnetic susceptibility. d) Mismatched $f = 1.5\%$ PG foam shows reduced perturbations, but still a significant susceptibility effect. e) $f = 4.0\%$ PG foam demonstrates improved susceptibility matching with the predicted $\sim 10\%$ tolerance in targeted volume fraction for water matching ($f = 4.5\%$). f) $f = 4.5\%$ PG foam demonstrates good susceptibility matching to water because it reduces off-resonance effects down to ± 1 ppm, relative to the ± 5 ppm off-resonance effects from air at the water interface.

Typical off resonance artifacts (Section 2.4) are seen in the EPI images of the air phantom in Fig 4.5. The long readout time of the EPI sequence results in increased T_2^* artifacts because the rotating spins have more time to lose coherence. The common “bullet” artifact is seen in the readout direction as expected and is accompanied by blurring and severe signal dropout. The use of susceptibility matching materials homogenizes the field, resulting in the reduction of artifacts in the PG foam and water phantoms.

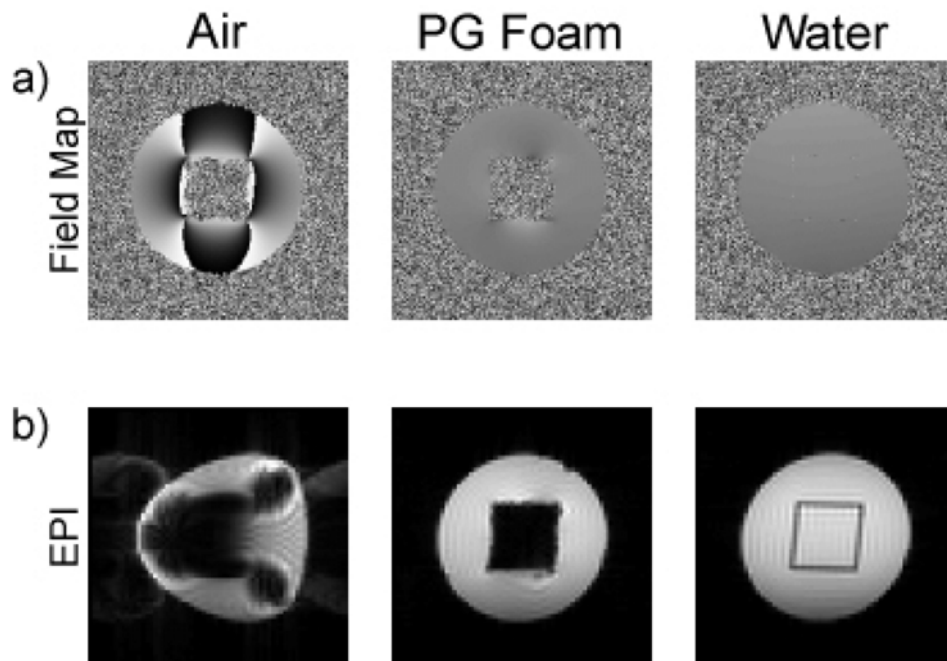


Fig 4.5: Field inhomogeneities cause artifacts in sequences with long readout times, such as EPI. Susceptibility matching materials such as PG foam and water minimize these artifacts.

4.3.2 PG Foam Conductivity

Q values were obtained of the head sized PG foams, PG powder, human heads and air (unloaded) in the 4T tuned MR head coil. A sample 4.5 L PG foam loaded in the coil is shown in Fig. 4.2b. Figure 4.6 shows that the regular foam and the PG foams have virtually the same Q and only a negligible effect on the coil Q value compared to the unloaded coil, indicating that the PG foams are non-conductive and add virtually no additional noise to the receiver coil. This is in contrast to the significant Q drop when the coil was loaded with conductive PG powder (not in a foam) or when loaded as normal with human heads ($N = 6$), which were significantly smaller in Q than the foams.

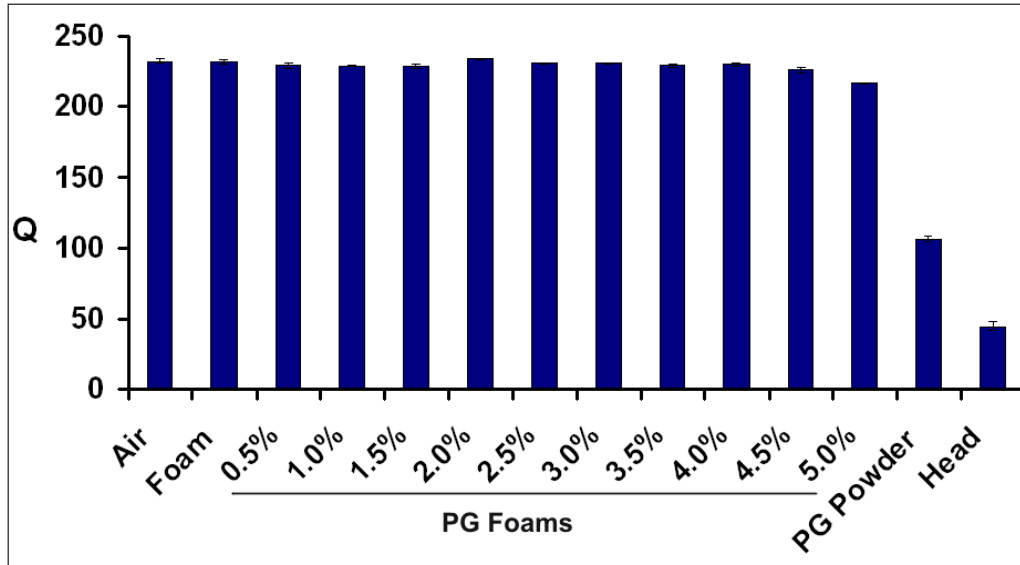


Fig 4.6: Q Measurements on a Varian 4T head coil. Q measurements show the PG foams to be nonconductive, similar to air or regular foams, and thus add no additional noise to the receiver coil. Q for conductive loads of PG powder, and human head are also shown for comparison. Load volumes were approximately 4.5 L.

4.3.3 PG Foam Heating

As a second corroborative test of conductance, the direct heating tests of the foam are shown in Figure 4.7. There were no discernible effects of heating ($|\Delta temp| \leq 0.2^\circ\text{C}$) over the courses of the heating tests. Figure 4.2b shows a sample setup of the PG foam in the coil for heating tests.

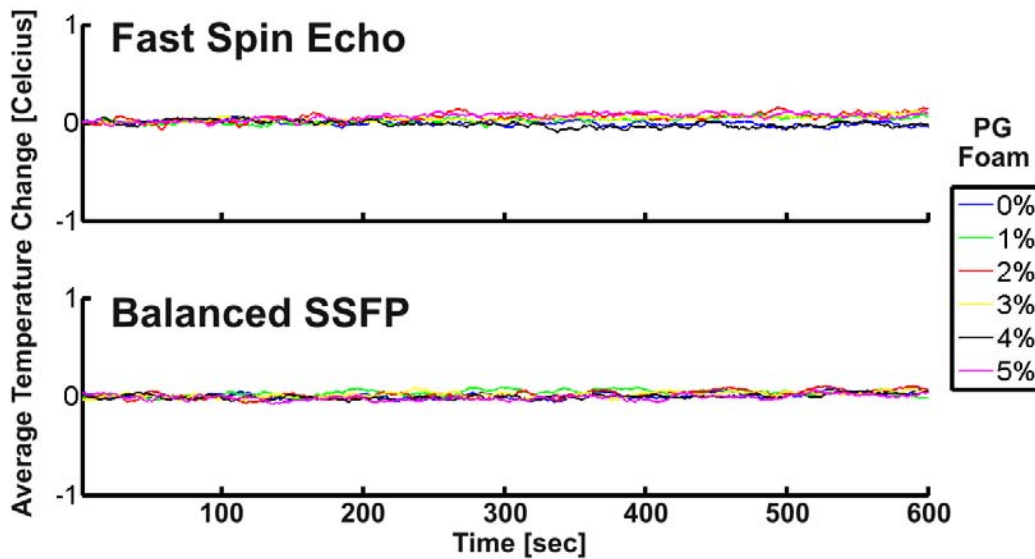


Fig 4.7: 10 minute temperature changes using (top) fast spin echo ($\alpha = 180^\circ$), and (bottom) balanced SSFP ($\alpha = 70^\circ$) pulse sequences indicates no heating in the foams. $|\Delta temp| < 0.2^\circ\text{C}$.

4.3.4 Field Maps of Modified PG Foams

Fig 4.8 shows representative field maps of the plasticizer-enhanced foams. The field maps are depicted as unwrapped field maps to highlight any field perturbations. As expected, the “dipole” effect in the plasticizer-enhanced 0% foam phantom has reduced perturbations compared to the air phantom due to the slight diamagnetic susceptibility of the additional plasticizer. The dipole effect also inverts signs near the $f = 3.9\%$ foam as predicted indicating susceptibility matching to the surrounding water.

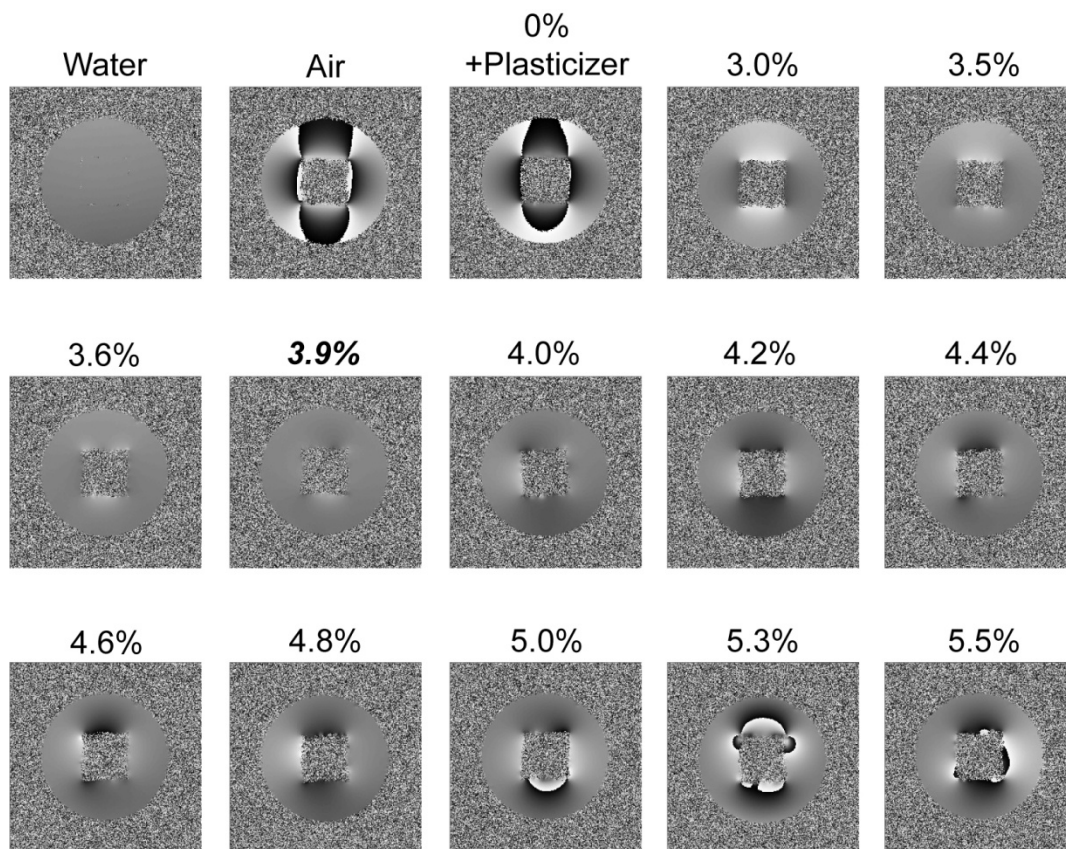


Fig 4.8: Unwrapped field maps of custom plasticizer-enhanced PG foams. The addition of a slightly diamagnetic plasticizer reduced f from 4.4% to 3.9%.

Magnified images (100x) of the 44 and 100 micron median diameter PG particles are shown in Fig 4.9. The larger particles provided viscosity relief during the PG foam manufacturing process by reducing the ratio of volume to surface area. In conjunction with the custom plasticizer, this enables the manufacturing of more homogeneous PG foams. In Fig. 4.10, field maps (as unwrapped phase difference maps) of the 100 micron PG foam blocks are compared with those of the 44 micron PG foam blocks to verify that the change in particle size did not change the volume fraction specification from $f = 3.9\%$ for susceptibility matching. Table 4.1 shows the σ values (mean \pm standard deviation) from the phantoms and verifies that the $f = 3.9\%$ phantoms lead to the best susceptibility matching. The difficulty for achieving good volume fraction uniformity in the PG foams increases with increasing volume fraction, which is reflected in the increasing standard

deviations of σ . Note that σ is geometry dependent and is useful for comparing results of experiments using identical phantom setups.

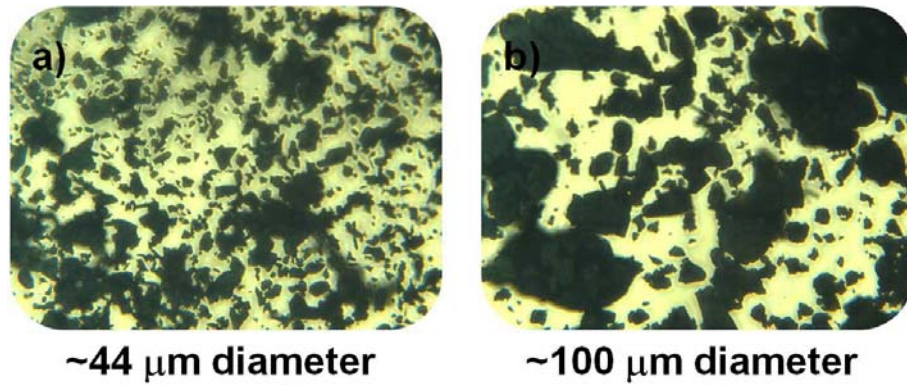


Fig 4.9: Increasing median particle size of PG from 44 μm to 100 μm reduces mixing viscosity during the PG foam manufacturing process.

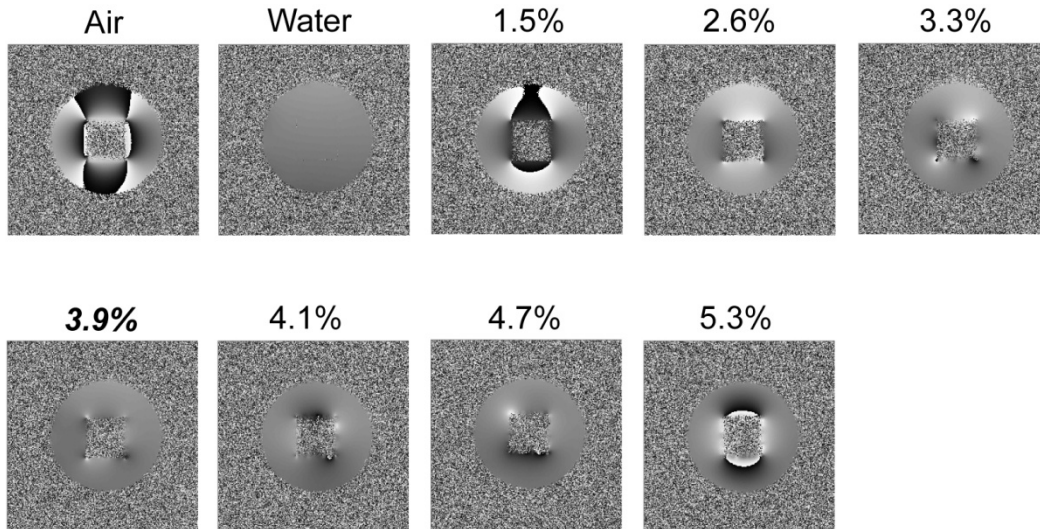


Fig 4.10: Unwrapped field maps of PG foams containing 100 micron median diameter particles. Increasing median PG particle size does not change volume fraction for susceptibility matching, reduces mixing viscosity during the manufacturing process, and improves homogeneity.

	σ (mean \pm standard deviation)	Doping Level
Air	1.32 ± 0.01	Underdoped
Water	0.18 ± 0.01	Perfect Match
1.5%	0.78 ± 0.01	Underdoped
2.7%	0.37 ± 0.07	Underdoped
3.3%	0.37 ± 0.20	Underdoped
3.9%	0.22 ± 0.08	Best Match
4.1%	0.32 ± 0.07	Overdoped
4.7%	0.33 ± 0.10	Overdoped
5.3%	0.45 ± 0.13	Overdoped

Table 4.1: Experimental field homogeneity metrics (mean \pm standard deviation) calculated for a range of 100 micron diameter PG foam phantoms. Dispersion or width of the field map histograms is represented by the σ values. The best susceptibility matching to water is seen near 3.9% volume

4.4 Discussion

Superconducting magnets can be passively shimmed to have the static B_0 field with 1-2 ppm uniformity over typical regions of interest (17). The remaining static field inhomogeneities are usually comprised of low order spatial variations that can be reduced through the use of similarly low order spherical harmonic active shim coils (46). Thus the main sources of static inhomogeneities in the B_0 field arise from objects with varying magnetic susceptibilities in the body or sample. Consequently, air-tissue and tissue-tissue boundaries in the body are unavoidable and typically uncorrectable sources of field gradients within the main field. These perturbations occur across all susceptibility boundaries (some with diminished magnitude due to gross geometry) and contain higher order spatial variations in the field that cannot be corrected by the lower order active shim coils (32).

Previously, other passive techniques have been introduced to reduce or eliminate the effects of these susceptibility boundaries. These methods include the use of pads of external diamagnetic fluids, such as water or perfluorocarbon (39-41). Water or perfluorocarbon pads can be used to surround the relevant tissue of interest because their magnetic susceptibilities are naturally close to those of human tissues. In effect, this moves the field gradients from the mismatched susceptibility boundaries out of the field of view or away from the region of interest. Perfluorocarbon has no intrinsic water signal and water can be doped with paramagnetic ions to have no MRI signal so as not to saturate the image. The disadvantage of this technique is the incompatibility with embedded RF coils, bulkiness, and lack of patient comfort. Of course, PG foam can only address field perturbations due to external air cavities; it cannot improve the magnetic field disturbance due to sinus cavities or lungs.

Others have used the field gradients arising from oral and aural shims of the strongly diamagnetic pyrolytic crystals in an attempt to directly compensate for inhomogeneities caused by air-tissue interfaces in the sinus and aural cavities (34-36).

However, it is difficult to compensate for the dipole-like field effects from the air cavities using the similarly dipole-like effects of the graphite shims at a distance away from the original source. This technique does have the advantage of improving the field in areas where the air cavity cannot be directly accessed or filled, but similar to an active shim, it cannot completely correct the higher order spatial variations. The active current-carrying coil methods have been shown to improve field homogeneity in the human prefrontal cortex (37,38), but has not been tested or modified for use in other body geometries and applications.

The uniformity of the main field is especially important in applications such as fat suppression. In MRI fat appears with a bright signal and can cover up relevant features in the region of interest. Fat suppression techniques in MRI are often particularly relevant around areas with natural susceptibility boundaries, such as the breast, head, back, and other extremities. Traditional fat suppression techniques include spectrally selective RF fat saturation pulses, short T_1 inversion recovery (STIR) imaging, 2 point Dixon, and 3 point Dixon/IDEAL techniques.

Spectrally selective fat saturation methods typically use the 3.5 ppm chemical shift between fat and water to exclusively excite and saturate the fat signal prior to MRI (47), or to excite only the water (spectral spatial). Because the chemical shift between fat and water is small, a uniform static field on the order of 1 ppm is required to correctly perform chemical shift selective RF pulses for fat suppression. Thus, these methods typically fail near areas with strong susceptibility mismatches (48), with either unreliable fat suppression or erroneous suppression of water (tissue) signal.

STIR methods use an inversion pulse to suppress fat by its short T_1 . While fat suppression can be uniform with STIR using a non-frequency selective pulse, any species with T_1 similar to fat, including contrast-enhanced tissue, is also suppressed (49). STIR typically has poor SNR performance (50) due to saturation from the inversion pulse. Frequency selective STIR pulse sequences do not suffer this SNR degradation, but again these methods require pristine 1 ppm field homogeneity.

A class of pulse sequence, often called 3-point Dixon methods, include IDEAL (Iterative Decomposition of water/fat using Echo Asymmetry and Least-squares estimation) methods (51,52), which generally use repetitive phase-shifted acquisitions (scans) and special reconstruction algorithms to account for field inhomogeneities to resolve chemical shift from field inhomogeneities. However, drawbacks to these methods include increased time necessary for acquisition and reconstruction (53). Specialized reconstruction techniques and software are also often used. Hence, it would be advantageous to improve field homogeneity so that these 3-point Dixon methods are not required

The use of the tissue susceptibility matched PG foam is especially relevant to applications such as breast MRI, for example, in which the air/tissue susceptibility boundary is accessible to the foam and requires an extremely uniform static field for proper fat suppression using the faster spectrally selective techniques. PG foam cushions

that would correct for a more uniform field to enable more robust frequency selective fat suppression could be pre-molded in various sizes for patient fit and comfort. Also, in breast MRI, the patient is typically imaged with a surface coil, in which SNR decreases as the distance away from the surface coil increases. Because PG foam is non-conductive, it is also compatible with embedded RF coils allowing maximal SNR from a given coil, something that could be unsafe with perfluorocarbon or doped water matching materials. In addition, in clinical practice, breast MRIs are often performed in conjunction with biopsy procedures. With the use of PG foam, the clinician can directly perform MR guided biopsies through the PG foam and around the surface coil without moving the patient. Also, anatomical features and positions can vary for each patient between scans depending on the placement of the breast. PG foam can be molded to the correct shape for a patient allowing for reliable and repeatable positioning prior to each scan.

PG foam also has applications in the general MR suite. In a typical MRI scan, the patient rests on a foam cushion on the exam bed and foam pieces may be used to secure the patient from moving during the scan. PG foam is lightweight and relatively inexpensive, so it can naturally replace other foams currently used in the MR suite, including the patient table bed. In addition, foam ear plugs are ubiquitous for patient safety inside the magnet bore and might be replaced with PG foam ear plugs, which may reduce susceptibility artifacts near the temporal lobe due to the air in the aural cavities.

Translating the PG foam from phantom applications to *in vivo* imaging raises two issues concerning compressibility and air gaps. First, using the foam as padding can result in compression for certain applications, such as under the head or back or inside the ear cavity. The change in volume will cause a change in density and PG volume fraction, and thus a susceptibility change. Our theory and phantom results show that a 10% error in volume fraction produces susceptibility matching to ~ 1 ppm, which would suggest that at least 10% compression would be tolerable for human imaging. The density and softness of the underlying foams used for the manufacturing of PG foams can be independently varied, so PG foams of varying compressibility and feel can be tailored towards specific applications, depending on whether pressure padding is required or the level of compression expected. Second, unlike the initial phantom experiments, the foam padding may not conform itself perfectly to the imaged body part, even if the foam is pre-molded, and thus air gaps are possible, which may be a source of dipole-like B_0 inhomogeneities. Solutions for simple ellipsoid patterns, such as spheres or cylinders have been published previously (9) and more complicated patterns can be predicted using a Fourier based method to calculate field perturbations from a heterogeneous magnetic susceptibility distribution (46,54,55). Because PG foam can be compressible and is relatively conforming, air gaps of less than a few millimeters are feasible, and our initial estimates of simple gap geometries suggest that the field homogeneities will be with a tolerable ~ 1 ppm.

In conclusion, we have described a tissue susceptibility matching pyrolytic graphite foam that will improve the homogeneity of the B_0 static magnetic field within the patient. PG foam reduces local inhomogeneities due to field gradients by moving the

susceptibility boundary away from the field of view or region of interest and it produces no MRI signal. By homogenizing the field, common susceptibility-induced artifacts, including signal dropout and image distortions can be reduced or mitigated. It is inexpensive, lightweight, non-conductive, does not heat, and safe to use with patients. It is also compatible with embedded RF coils. Future work will include developing foams for use in specific applications, such as in breast MRI, cervical spine, other extremity imaging applications, and spectroscopy.

Chapter 5

Frequency Selective Fat Suppression

5.1 Introduction

Fat suppression techniques are commonly used in MRI, because fat can often obscure subtle clinical features in the region of interest. A common method of fat suppression involves frequency (or spectrally) selective saturation techniques, which utilize the 3.5 ppm chemical shift between fat and water to exclusively saturate the fat signal prior to data acquisition (47), or to exclusively excite the water (56). A uniform static field of better than 1 ppm is required for robust chemical shift selective fat suppression. Thus chemical shift selective fat suppression often fail near areas with large field perturbations arising from mismatched magnetic susceptibility boundaries (48) resulting in either unreliable fat suppression or even erroneous suppression of water (tissue) signal.

A common challenge is robust fat suppression near the skin. The 10 ppm susceptibility difference between air and tissue results in field gradients near the skin and air-filled cavities. These air-tissue field gradients make fat suppression particularly challenging in the breast, head, back, and other extremities. The field disturbance from air-tissue interfaces can also cause other significant MRI artifacts including intravoxel dephasing, distortion, blurring, and voxel shifts (9). Certain types of pulse sequences, such as gradient recalled echo imaging (GRE), echo planar imaging (EPI), and balanced steady state free precession (bSSFP), are particularly sensitive to these B_0 field inhomogeneities. Other B_0 -sensitive MR applications include blood oxygen level dependent (BOLD) contrast (57), extremity MRI (58), MR spectroscopy (MRS) (40,59), and temperature mapping during RF or HIFU interventional treatment (60). The absolute sizes of the field perturbations scale with B_0 field strength, which makes artifact-free imaging at high fields a challenge. Still, it is important to realize that fat suppression remains a significant challenge even at lower field strengths since the off-resonance and the competing chemical shift *both* scale linearly with field strength.

The most common method to mitigate field inhomogeneity is to shim the region of interest (ROI), using active low-order spherical harmonic shim coils and gradient shims to correct for the field perturbations. Unfortunately these shim coils cannot robustly correct for high spatial frequency perturbations (31-33), because standard shim coils must be larger than the patient, and large DC coils are physically restricted to generating only low spatial frequency field patterns deep within a patient (9).

A simple, passive, and direct method to improve static field homogeneity near an air-tissue interface is to displace the air with a tissue susceptibility-matched material. If the matching material is thick enough, it effectively moves the field gradient *outside* the patient. Previous fluid susceptibility matching agents include perfluorocarbon, barium sulfate doped water, and Kaopectate (39-41).

We previously introduced the first lightweight (non-fluidic) magnetic susceptibility matching material for MR applications. Here, we doped closed-cell polyurethane foams with pyrolytic graphite (PG) microparticles to match the magnetic susceptibility of human tissue. We showed that composite magnetic susceptibility of the pyrolytic graphite foam ($\chi_{PG\ foam}$) is

$$\chi_{PG\ Foam} = \chi_{Total}f + \chi_{Foam}(1 - f) \text{ [ppm]}. \quad (\text{Eq. 5.1})$$

where $\chi_{Total} = -204$ ppm is the average susceptibility of the anisotropic components of pyrolytic graphite, χ_{Foam} is the base susceptibility of the polyurethane foam (typically equivalent to air), and f is the volume fraction of the pyrolytic graphite in the foam. We demonstrated experimentally that PG foam is lightweight, nonconductive and does not heat. The PG foam creates no MRI signal and no MRI noise and it is transparent to the RF transmit and receive coils. It safe for patient use and is also compatible with embedded RF coils (61). The unique advantages over other susceptibility matching agents are reduced density, ease of shaping, and embedded RF coil compatibility.

Here we perform the first experimental demonstration that PG foam is effective for minimizing field perturbation in a small group of healthy volunteers. This clearly shows that the inevitable air gaps between a standard-shaped cushion and the volunteers do not ruin the susceptibility matching. We also demonstrate experimentally improved frequency selective fat suppression in this group of normal volunteers. These are two important and practical proof of concept experiments. Specifically, we show experimentally that a composite PG foam cushion reduced field perturbations in both phantom and in the posterior neck. We compared simulated and measured field maps. We verified experimentally that the PG foams added no additional noise to the receive coil. We also compared the relative improvements in field uniformity using PG foams and targeted shims in healthy volunteers. We also demonstrated improvements in the robustness of frequency selective fat suppression techniques in both phantom and *in vivo* data.

5.2 Methods

5.2.1 PG Foam Construction and SNR

3D Anatomical Models

Various high resolution (better than 1 mm isotropic resolution) 3D volume MR images were acquired of the head, neck, and other various ROIs. Anatomic MRI data was then rendered into hollow molds of the ROI in SolidWorks (Waltham, MA). Examples of the 3D mold designs are shown in Fig. 5.1. Molds were printed out on a ZPrinter Model 150 3D printer (ZCorp, Burlington, MA), hardened with an epoxy infiltrant, and filled with casting plaster for durability. A final acrylic coating was applied to provide a non-porous finish on the mold. A sample neck mold is shown in Fig. 5.2.

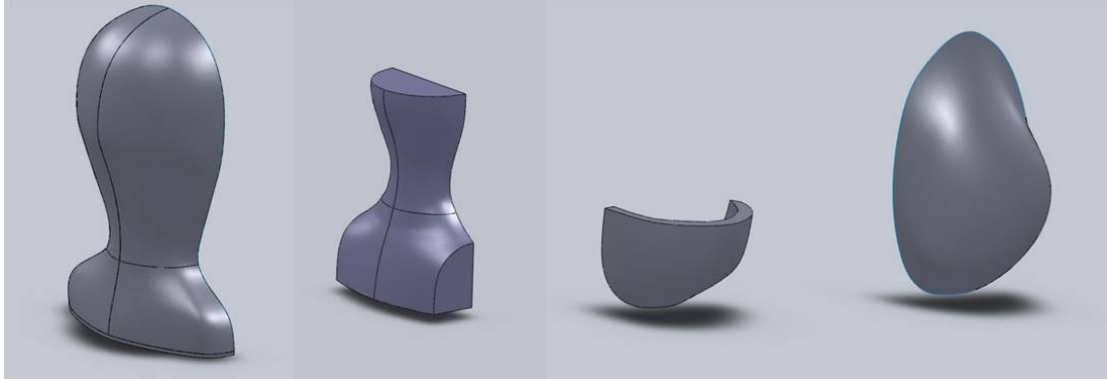


Fig 5.1: Examples of anatomical 3D mold models for the head, neck, and breast. Molds were created from high resolution MRI data.

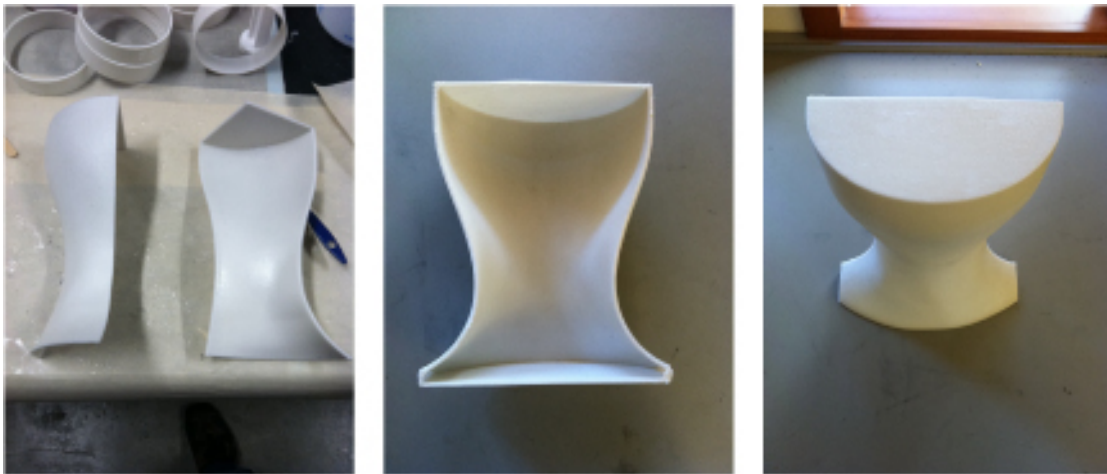


Fig 5.2: Various views of prototype anatomical neck mold for casting PG foam neck cushions. A 3D printer was used to create the neck mold in several pieces and epoxied together.

Foam Materials

Custom pyrolytic graphite (PG) foam blocks and neck cushions were created by dispersing high purity PG powder (Asbury Carbons, Asbury NJ) into a closed-cell, two-component polyurethane polymer foam system (Silpak, Inc., Pomona, CA). PG particles ranged from 44 to 110 microns in diameter. PG powder was uniformly dispersed into one of the foam components prior to combining. A custom plasticizer (Silpak, Inc., Pomona, CA) was also added both to reduce the viscosity of the initial foam slurry to facilitate homogeneous mixing and to create softer foams for patient comfort. The foam slurry was then poured into custom built plastic molding boxes and allowed to rise and cure. For the neck cushions, a 3D-printed standardized neck mold was placed in the molding box prior to pouring the slurry to create a generic human neck cushion. The foams were then shaped to fit into a phantom or a receive coil. A set of flat, 1.5" thick PG foam rectangular pads were also added to support the lower neck and the shoulders.

Volume Fraction Details

The susceptibility of the base un-doped foam was equivalent to the susceptibility of air ($\chi_{\text{Foam}} = \chi_{\text{Air}} = 0.36$ ppm) (61). The addition of the custom plasticizer modified the susceptibility of the base foam from minimally paramagnetic $\chi_{\text{Foam}} = \chi_{\text{Air}}$ to a slightly diamagnetic $\chi_{\text{Foam}} = -1$ ppm. Based on our theoretical calculations (61), we targeted foams with volume fraction $f = 3.9\%$ to match human tissue (or water) susceptibility of -9 ppm (9). PG volume fraction was controlled by dispersing a calculated mass of PG (based on its known 2.26 specific density) to achieve the final target volume fraction.

SNR Measurements

A cylinder of MnCl_2 -doped water was used as an SNR phantom. The water was doped to simulate tissue relaxation times (43). Q changes observed with MnCl_2 solution in a standard volume head coil indicated minimal loading of the RF coil, which will emphasize any potential noise added by the PG foams. Gradient echo images ($N=15$) were acquired with and without ~ 3.5 liters of tissue susceptibility matching PG foam blocks to pack a standard volume head coil. The FOV of the 256×256 images was $25.6 \times 25.6 \text{ cm}^2$ in-plane ($1.0 \times 1.0 \text{ mm}^2$ spatial resolution) with 3 mm slice thickness. TR/TE of the gradient echo images was 261.9/4 ms. Signal and noise values for each set were calculated to generate SNR values (62).

5.2.2 Frequency Selective Fat Suppression in Phantoms and *In Vivo*

Phantom Construction

Custom fat suppression phantoms were built to quantify field gradients near the susceptibility interfaces. Sets of two-compartment plastic apparatuses were constructed using a rectangular container ($58 \times 58 \times 150 \text{ mm}^3$) mounted inside of a larger cylindrical container (152 mm diameter, height). The containers were oriented orthogonal to the B_0 field. The surrounding cylindrical compartments were filled with cooking oil to create a fat region in the phantom. The smaller rectangular containers were filled with air, MnCl_2 -doped water, or PG foam blocks ($N = 4$ for each case) to create the relevant susceptibility boundaries.

Simulated Phantom Field Mapping Calculations

A spatial-Fourier transform-based method was implemented in Matlab to calculate field perturbations from a heterogeneous magnetic susceptibility distribution (46,63). This was used to simulate the field inhomogeneities caused by both susceptibility unmatched (equivalent to air) and matched regions (equivalent to water or PG foams) within the fat regions of the phantoms. The entire fat phantom was simulated and 2D coronal slices were analyzed. The field of view (FOV) of the 256×256 simulated images was $22.4 \times 22.4 \text{ cm}^2$ in-plane ($0.875 \times 0.875 \text{ mm}^2$ spatial resolution) with 3.75 mm slice thickness.

Volunteer info and informed consent

Six healthy volunteers (5 males, 1 female, ages 21-31) were recruited for this experiment. Informed consent was obtained under the human subjects protocol approved by the Institutional Review Board (Committee for the Protection of Human Subjects) at the University of California, Berkeley.

Field Mapping

For the fat suppression phantoms, coronal off-resonance field maps were acquired on a 3T GE Signa scanner (General Electric, Waukesha, WI, USA) using a standard GE IDEAL (Iterative Decomposition of water/fat using Echo Asymmetry and Least-squares estimation) pulse sequence and a standard head coil. The field of view (FOV) of the 256x256 magnitude images was 22.4 x 22.4 cm² in-plane (0.875 x 0.875 mm² spatial resolution) with 3.75 mm slice thickness. The TR of the IDEAL sequence was set at 6.3 ms, and utilized various TE (base TE = 2 ms). A standard GE auto-shimming protocol was used and the RF excitation pulse was verified to be centered on the water peak. An additional doped water bath was placed in the receive coil with all the fat phantoms to ensure that the RF pulse was properly centered. Field maps were auto-computed using IDEAL data and built-in iterative reconstruction and phase unwrapping algorithms.

Sagittal 3D multi-slice gradient echo images of the neck were acquired with and without a PG foam neck cushion to produce off-resonance field maps from a 3T Siemens TRIO scanner (Siemens Medical Systems, Erlangen, Germany) using a standard Siemens field mapping pulse sequence and a modular head, neck, and spine receive coil system in the surface coil configuration. The FOV of the 256x256 images was 25.6 x 25.6 cm² in-plane (1.0 x 1.0 mm² spatial resolution) with 3 mm slice thickness. The field mapping sequence acquired a series of two similar 3D gradient echo scans with the same FOV to compute the off-resonance field maps. TR of both scans was 488 ms. TE was 4.92 and 7.38 ms for the two scans, respectively. Separate field maps were acquired using the full FOV as the shim volume and after adjusting the shim to cover a reduced FOV, including the cervical spine and the posterior neck. A standard Siemens auto-shimming protocol, including standard second order shims (after any cushion was placed), was used and the RF excitation pulse frequency was verified to be centered on the water peak for each case.

Fat Suppression

Standard gradient echo images with and without frequency selective fat suppression were acquired to demonstrate the effect of field inhomogeneities in the fat phantoms. The FOV of the 256x256 magnitude images was again 22.4 x 22.4 cm² in-plane (0.875 x 0.875 mm² spatial resolution) with 3.75 mm slice thickness. TR/TE of the gradient echo images was 600/3.5 ms. A standard GE auto-shimming protocol was again used and the RF excitation pulse frequency was verified to be centered on the water peak as before.

Standard T_1 -weighted FLASH (Fast Low Angle Shot, a type of gradient echo sequence) images with and without frequency selective fat suppression were acquired to demonstrate the effect of field inhomogeneities with and without the use of PG foam neck cushions in the posterior neck. The FOV of the 256x256 magnitude images was again 25.6 x 25.6 cm² in-plane (1.0 x 1.0 mm² spatial resolution) with 3 mm slice thickness. TR/TE of the gradient echo images was 589/2.46 ms. Identical auto-shimmed regions (full FOV and cervical spine) were prescribed as in the previous *in vivo* field maps. A second set of FLASH images with and without fat suppression were acquired with RF excitation center frequencies offset by ± 1 ppm to demonstrate the increased robustness of the fat suppression using the PG foam neck cushions.

5.2.3 Data Processing

The field map simulations, measured field maps, histograms, SNR, and statistical analyses were performed using custom in-house MATLAB code (Mathworks, Natick, MA, USA). The off-resonance field maps were computed using a standard technique from the gradient echo phase maps by dividing the phase accrual data by ΔTE (44), following phase-unwrapping (64). The distribution of each phantom or *in vivo* field map was described by a histogram, and σ (standard deviation), 4σ (a standard descriptor of 95% width of a normal distribution), and the percentage of voxels outside the ± 1 ppm threshold were calculated as measures of dispersion to characterize field homogeneity (40). Paired Wilcoxon signed-rank, two-factor ANOVA and Tukey multiple comparison tests were used for statistical comparisons. A p-value less than 0.05 was considered significant.

5.3 Results

5.3.1 PG Foams and SNR

The PG foam blocks have $f = 3.9 \pm 0.2\%$ and a final density of 0.26 g/mL. Figure 5.3a shows a large PG foam block that has been shaped into the smaller rectangular blocks used for both the fat suppression phantom and the SNR experiments. The custom molded PG neck cushion was shaped to fit into the head, neck, and spine receive coil setup (Fig. 5.3b-d). The neck foam was shaped such that at least one inch of PG foam was in contact with the posterior neck/cervical spine region and the rectangular pads were used to extend the PG foam coverage down the c-spine. The PG foam packed phantoms had virtually identical SNR to the unpacked phantoms, 101 ± 4.6 compared to 102 ± 4.8 (mean $\pm \sigma$), indicating that no noise was added by the PG foams.

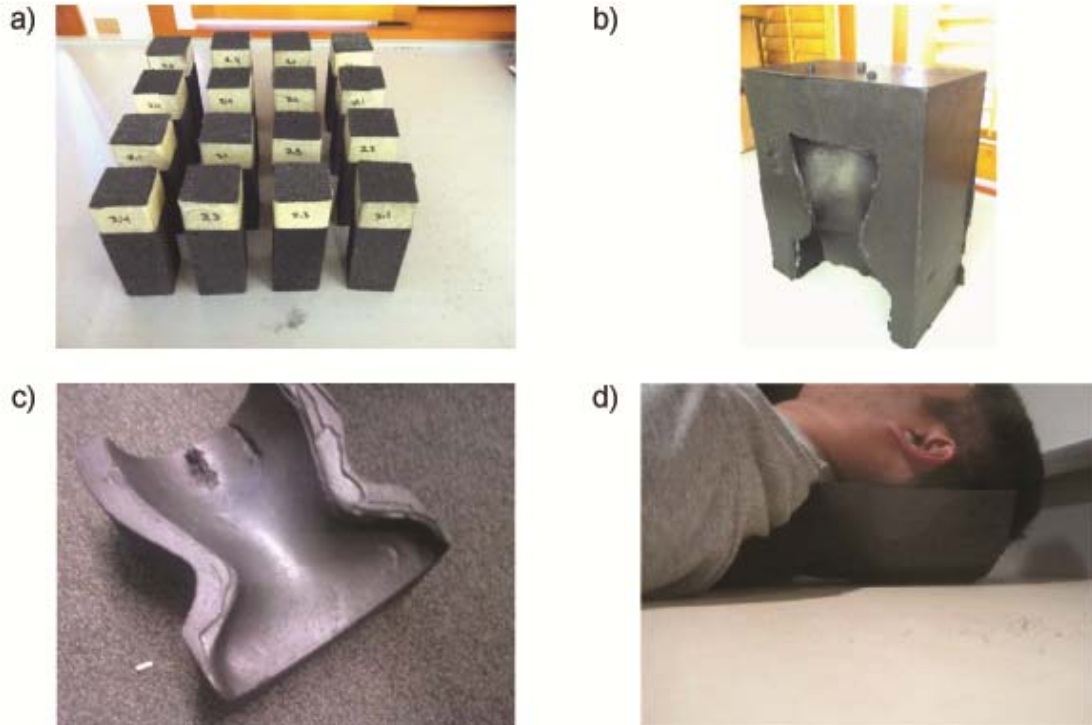


Fig 5.3: (a) PG foam blocks ($56 \times 56 \times 150 \text{ mm}^3$) shaped for the phantom fat suppression and SNR experiments. (b) Custom molded PG foam neck cushion with the 3D printed neck mold removed ($18 \times 31 \times 38 \text{ cm}^3$). (c) PG foam neck cushion shaped to fit into the head, neck, and spine receive coil setup. (d) Representative example of a subject resting on the cushion. The same neck cushion was used for each subject in this study.

5.3.2 Fat Phantom Field Maps and Fat Suppression

Figure 5.4 shows simulated off-resonance field maps for the (a) susceptibility unmatched and (b) matched fat phantoms. In the field maps, the unmatched susceptibility interface predicts a classic dipole field pattern that should appear outside the air compartment in the fat region. The field maps also predict that the water and PG foam compartments should produce little to no field perturbations. The computed histograms from the simulated field maps are shown in Fig. 5.4c-d. When an unmatched susceptibility interface was simulated, the field distribution was neither narrow nor symmetric.

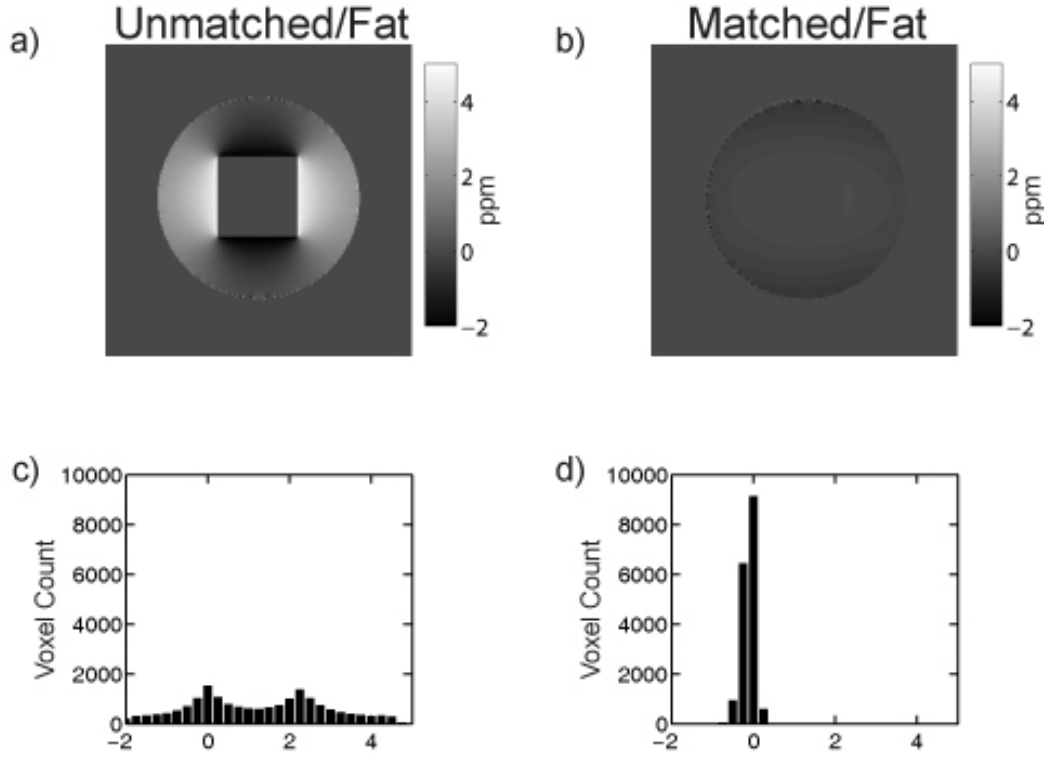


Fig 5.4: Simulated field maps of the fat phantoms containing (a) unmatched and (b) matched susceptibility distributions predicting the field inhomogeneities. (c)-(d) Corresponding histograms of the simulated field maps showing the field distributions. Static field homogeneity was significantly improved in the susceptibility matching case to be within the critical ± 1 ppm threshold for robust fat suppression. Note that the field distribution in (c) was predicted to be broad and asymmetric about zero, but became narrow and symmetric in (d).

The field maps are compared for a representative set of the (a) air, (b) water, and (c) PG foam filled fat phantoms are shown in Fig. 5.5a-c. Figure 5.5a shows the field map predicted by the simulations, with excursions up to ± 4 ppm. Water and PG foam filled phantoms show good susceptibility matching, with field excursions within ± 1 ppm (Fig. 5.5b-c). The corresponding histograms have 4σ values of 4.85, 0.93 ppm, and 1.18 ppm for air, water, and PG foam, respectively (Fig. 5.5d-f). It is important to note that *the percentage of voxels within the critical robust fat suppression threshold (± 1 ppm) increased from 44% (with no PG foam) to 99% (with PG foam)*. The failure of robust frequency selective fat suppression near air is seen experimentally in Fig. 5.6, whereas the fat suppression is robust when the phantom is surrounded by PG Foam.

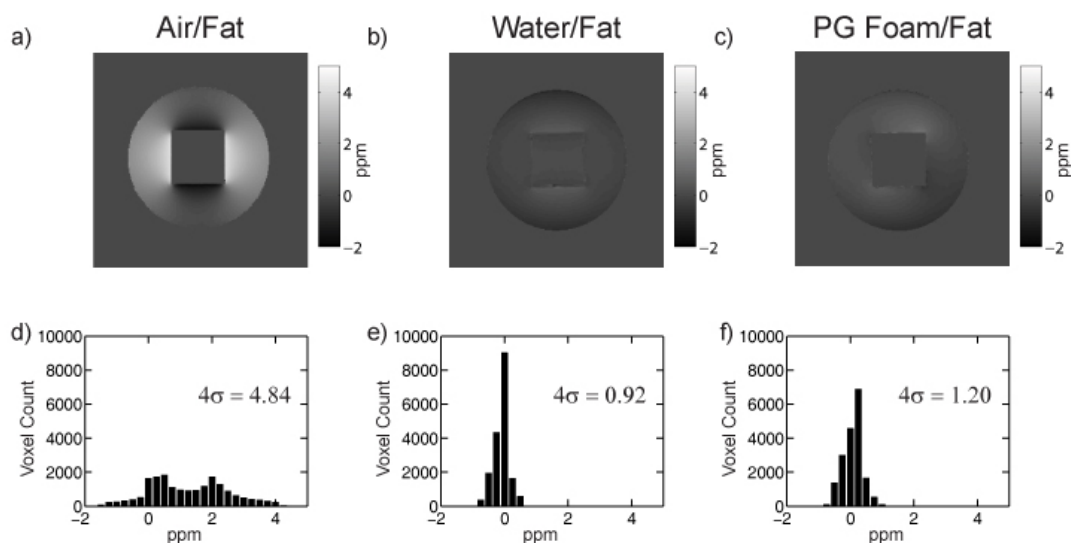


Fig 5.5: Representative experimental field maps of the fat phantoms containing (a) air (b) water, and (c) PG foam, showing the field inhomogeneities. (d)-(f) Corresponding histograms of the field maps showing the field distributions and the 4σ values. Static field homogeneity was significantly improved with the use of the susceptibility matching water and PG foam blocks to be within the critical 1 ppm threshold for robust fat suppression. Note that the field distribution in (d) was broad and asymmetric about zero, but became narrow and more symmetric in (e) and (f).

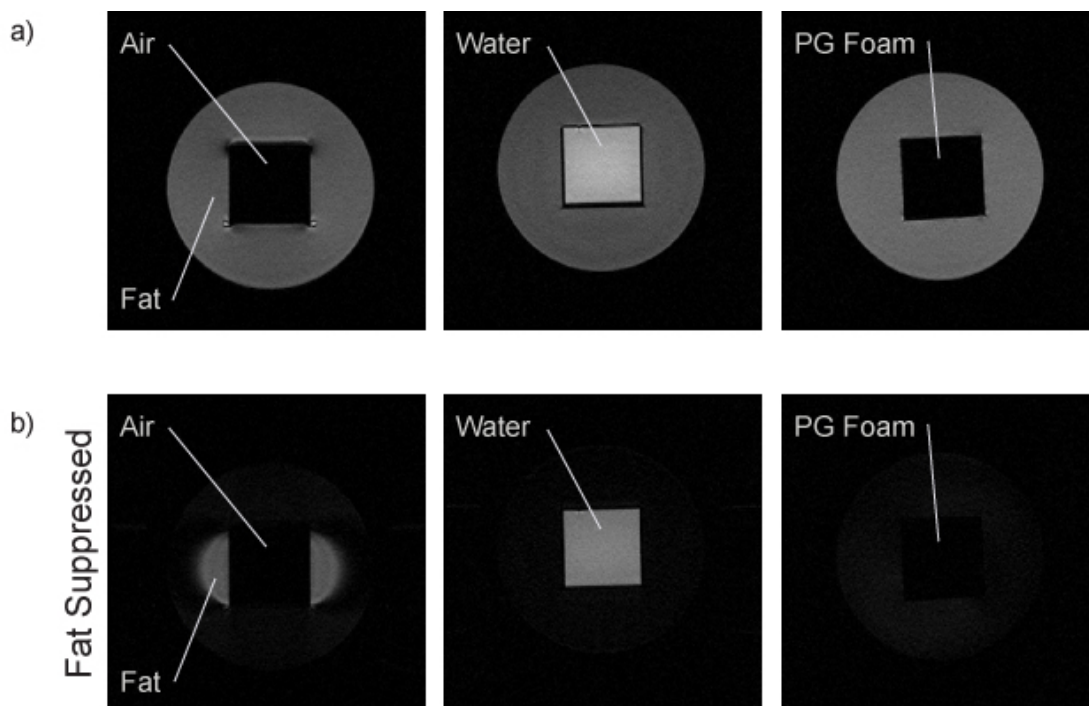


Fig 5.6: (a) Gradient echo MR images of a fat phantom consisting of an oil-filled compartment surrounding compartments of air, water, and PG Foam. (b) Fat signal was not properly suppressed following a frequency selective fat saturation pulse in areas of poor field homogeneity near the air/fat boundary. Susceptibility matching water and PG foams enabled more robust fat suppression in the fat phantom.

5.3.3 *In Vivo* Field Maps and Fat Suppression

Figure 5.7 shows an example of the two *in vivo* shim volumes used for each volunteer on a T₁-weighted central sagittal slice. The global (full FOV) shim volume (Fig. 5.7a) was centered on the first cervical vertebra (C1). The smaller, local shim volume was prescribed around the length of the cervical spine (vertebrae C1-C7) and the posterior neck region (Fig. 5.7b). A typical size for the adjusted field of view was 200x125 mm².

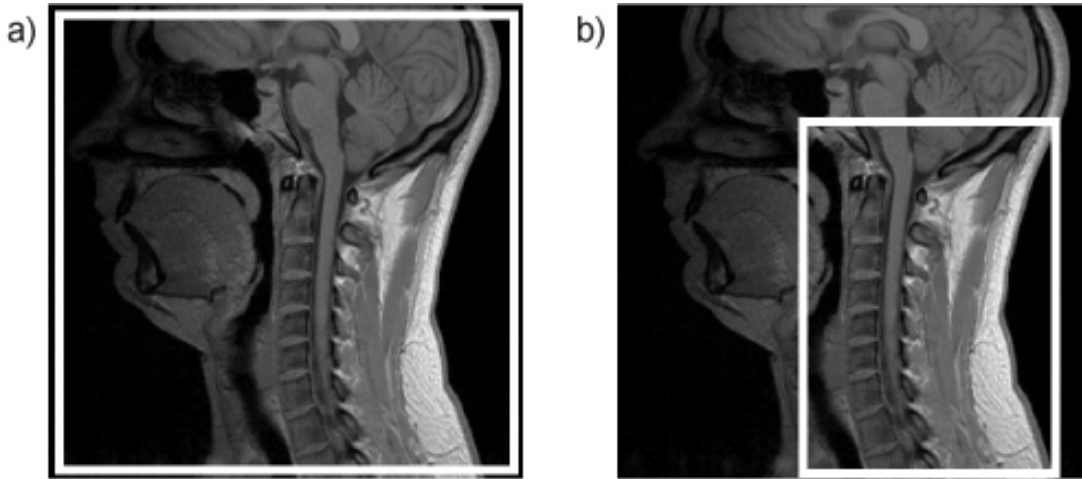


Fig 5.7: Two sample shim volumes used for acquiring field maps and T₁-weighted FLASH images: (a) Global shim volume corresponding to the full FOV (256 x 256 mm²) and (b) Local shim volume corresponding to a reduced FOV encompassing the cervical spine and posterior neck (200 x 125 mm²).

The full FOV shim volume field maps and histograms for one subject with a regular cushion and a PG neck cushion are shown in Fig. 5.8. Field inhomogeneities up to ± 2.5 ppm using the regular cushion are reduced to ± 1 ppm with the PG cushion. The 4σ values are similarly reduced from 2.48 to 1.42 ppm and indicate a more uniform static field. The use of PG foam also increases the percentage of voxels that satisfies the critical ± 1 ppm threshold from 84% to 98%. Table 5.1 shows the averaged values of the 4σ and the percentage of voxels greater than ± 1 ppm values for both the full FOV and smaller FOV shim volumes with and without PG foam. The addition of a PG foam neck cushion significantly ($p < 0.05$) reduced the dispersions of the field distributions for each volunteer, as well percentage of voxels outside of the critical ± 1 ppm threshold. In this experiment, the use of a smaller FOV shim volume did not consistently improve the uniformity of the static field.

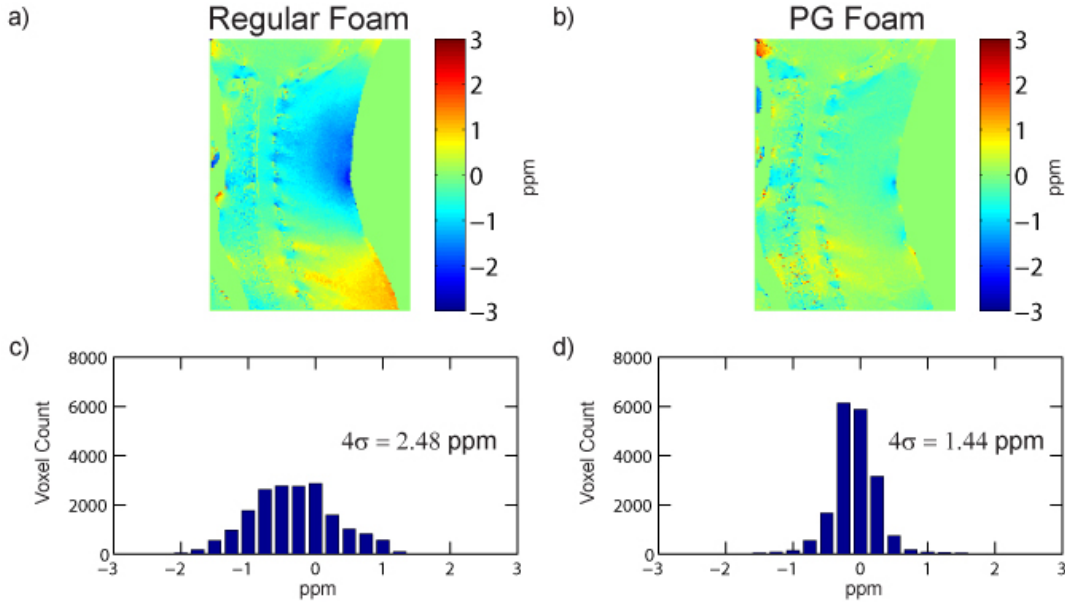


Fig 5.8: Representative experimental color-coded sagittal field maps of the cervical spine and posterior neck ROI using (a) regular foam padding and (b) a PG foam neck cushion, showing the field inhomogeneities. (c)-(d) Corresponding histograms of the field maps showing the field distributions and the 4σ values. The static field homogeneity was significantly improved with the use of the susceptibility matching PG foam neck cushion. The use of PG foam reduces the percentage of voxels outside of the critical ± 1 ppm threshold from 15.7% to 2%.

N=6		Control		PG Foam	
Field Homogeneity Metric	Units	Global Shim	Local Shim	Global Shim	Local Shim
$ \text{Voxels} > 1\text{ppm}$	[%]	24.2 ± 7.6	25.3 ± 16.3	4.9 ± 2.9	5.9 ± 4.2
4σ	[ppm]	3.07 ± 0.54	3.02 ± 0.60	1.92 ± 0.46	1.95 ± 0.50

Table 5.1: Experimental field homogeneity metrics (mean \pm standard deviation) calculated for all subjects with and without the susceptibility matching PG foam neck cushion using either global (full FOV) or local (reduced FOV) shim volumes. The percentage of voxels magnitudes greater than 1ppm indicates the relative number of voxels that fail the ± 1 ppm threshold for robust frequency selective fat suppression. Dispersion and $\sim 95\%$ voxel width of the field map histograms are represented by the 4σ values. The addition of a PG foam neck cushion significantly ($p < 0.05$) reduced the dispersions of the field distributions for each volunteer, as well percentage of voxels outside of the critical ± 1 ppm threshold. In this experiment, the use of a smaller FOV shim volume did not consistently improve the uniformity of the static field.

Figure 5.9 shows the failure of robust frequency selective fat suppression in one set of the *in vivo* T_1 -weighted FLASH images. Regions of failed fat suppression, signal dropout, and reduced SNR are clearly evident in the fat suppressed image with the regular cushion, but are not seen in the corresponding regions in the image acquired using the PG foam neck cushion. In Figure 5.10, changing the center frequency of the RF excitation pulse also demonstrates increased robustness of both fat suppression and water excitation with a susceptibility matched PG foam. A +1 ppm offset in the RF center

frequency combined with the field perturbations produced by the susceptibility interface was enough to shift the regional fat resonance frequency outside the bandwidth of the fat saturation pulse with the regular cushion, resulting in failed fat suppression. The artifacts are reduced with the use of the PG foam neck cushion (Fig 5.10b).

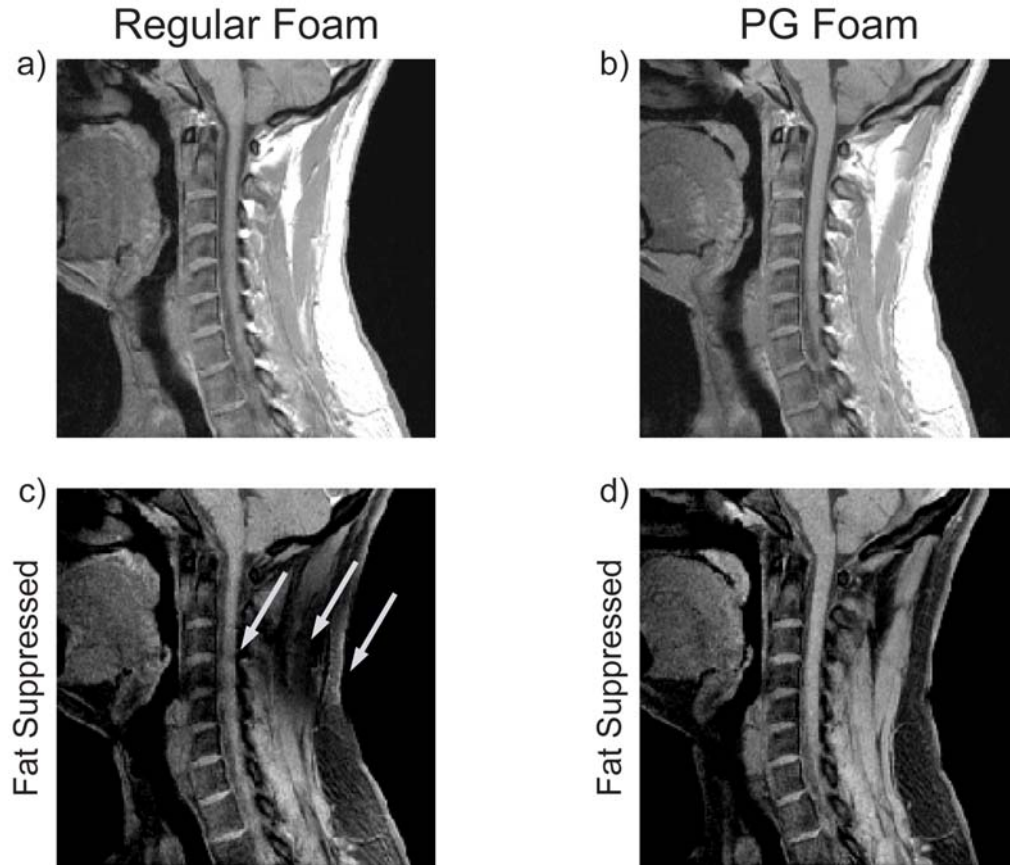


Fig 5.9: Representative T₁-weighted FLASH images of one of the volunteers using (a) regular foam padding or (b) a PG foam neck cushion. (c) The frequency selective fat suppressed image showed signal dropout, reduced SNR, and failed fat suppression in the region of poor static field homogeneity. (d) The susceptibility matching PG foam neck cushion demonstrated robust fat suppression and fewer susceptibility-induced artifacts.

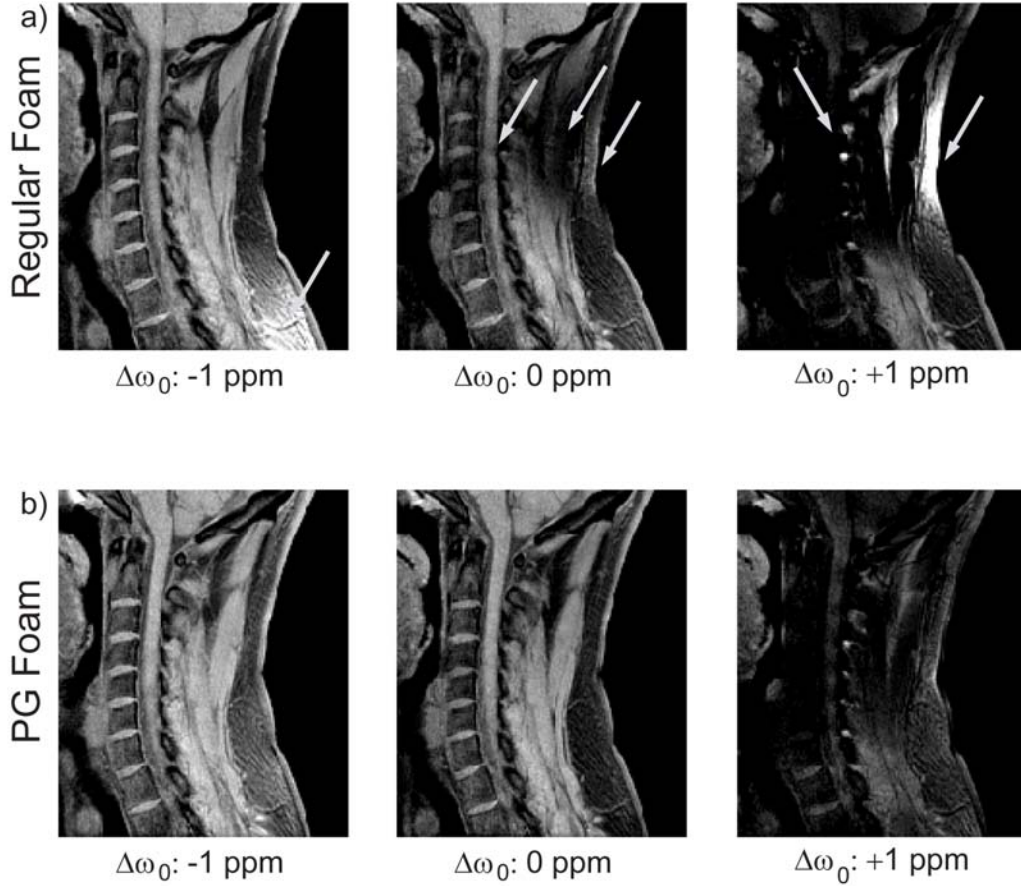


Fig 5.10: (a) Representative Frequency selective fat suppressed T_1 -weighted FLASH images of one of the volunteers using regular foam padding with RF center frequency offsets ($\Delta\omega_0$) of -1, 0, and +1 ppm showed signal dropout, SNR loss, and failed fat suppression. (b) The same images using a susceptibility matched PG foam neck cushion demonstrated a marked improvement in the robustness of the fat suppression. Note that the tissue signal is reduced in both cases when $\Delta\omega_0 = +1$ ppm due to the change in resonance frequency, but the water excitation is significantly more uniform using the PG foam.

5.4 Discussion

5.4.1 Alternative Methods of Fat Suppression

Another common fat suppression method is short- T_1 inversion recovery (STIR) pulse sequences, which time the RF excitation pulse at the null point of fat following an inversion pulse. This is effective since fat typically has much shorter T_1 compared to other tissues. Using a non-frequency selective inversion pulse, STIR can achieve robust fat suppression, insensitive to static field homogeneity. However, STIR sequences typically have reduced SNR (50) because the water signal is partially saturated by the inversion pulse. Moreover, the saturation effect can be prohibitively severe for contrast-enhanced blood or tissues, where gadolinium agents produce T_1 's similar to fat (49). The inversion pulse for STIR can be made spectrally selective (65) so that SNR of other T_1 's

is not degraded. However, these methods are now vulnerable to B_0 field inhomogeneity, because of the frequency selective pulse.

Three-point Dixon methods (including IDEAL, Iterative Decomposition of water/fat using Echo Asymmetry and Least-squares estimation), use multiple image acquisitions with distinct phase accrual to resolve a fat and water images in the presence of an unknown B_0 inhomogeneity (51,52). These methods can be robust in the presence of modest field inhomogeneity but do require increased acquisition time (53). However, this technique could be more effective when used with an effective susceptibility matching material.

5.4.2 Static Field Shimming

The low spatial frequency spherical harmonic shim coils available on standard MR scanners are simply too large to correct for high spatial frequency magnetic fields generated near abrupt air-tissue boundaries. Here we found that local shimming (over the ROI) did not consistently improve the field homogeneity relative to global or local shimming. We recommend both susceptibility matching and local shimming for the best achievable field shim. Other susceptibility matching materials, such as perfluorocarbons, Kaopectate, or barium sulfate (39-41), can match human susceptibility and they give off no MRI signal. But none of these fluids are lightweight and none are compatible with embedded RF electronics.

Different materials and techniques have been used to reduce those field gradients at a distance. Passive crystalline pyrolytic graphite shims (34) lack adjustability once placed inside the mouth. Active coil loops have been placed orally to improve the field homogeneity near the sinus cavities (34,37), but there may be space constraints, as well as safety concerns with the torque between the active shims and the B_0 field. Sets of localized external current-carrying coils have also been used to dynamically compensate for inhomogeneities in the human prefrontal cortex (38). This method requires additional hardware and electronics to homogenize the field for each specific subject and ROI. It is also worth noting that these techniques can be used concurrently with PG foam to minimize susceptibility-induced field gradients.

5.4.3 PG Foam Air Gaps and Compression Tolerances

Two important practical considerations for using PG foams are unavoidable air gaps and unavoidable compression of the PG foams. Both effects could reduce susceptibility matching, so it is prudent to estimate tolerances for each. Here, magnetic field solvers using finite element or Fourier based methods were indispensable (46,63) for verifying that air gaps of less than a few millimeters are well tolerated in our experimental conditions. The physical intuition behind this observation is best appreciated by modeling the air gap as a sphere of air of radius a in a region of homogeneous susceptibility. That is, we are assuming a thick layer of PG foam but a small air bubble near the skin. These resulting dipole field perturbations are known to fall off as

$\Delta\chi \cdot B_0(a/z)^3$ where a is the radius of the air dipole and z is the distance away from the center of the air gap. Hence, the field perturbation falls off by a factor of 8 just two radii away from the source. This obtains a very practical rule of thumb: since the peak disturbance of air is ± 5 ppm, the maximum field disturbance is $\sim 5/8$ ppm just one diameter away from the air gap source. So an air gap of 2 mm implies that the field just 2 mm deep in the tissue is homogeneous enough to allow for robust spectrally selective RF pulses.

A change in volume due to compression of the PG foam will cause a change in density and PG volume fraction, and thus a change in the susceptibility. We have previously shown that a 10% error in volume fraction produces susceptibility matching to ~ 1 ppm, so at least 10% compression would be tolerable (61). PG foams of varying compressibility and feel can also be tailored towards specific applications, depending on the level of compression anticipated. Fortunately, in this study, problems arising from air gaps or compression were not observed with the standardized PG neck cushion. Further study in a clinical setting is recommended.

The major advantage of using PG foam over other passive fluid susceptibility matching techniques is the compatibility with RF coils. SNR is improved when the receive coil matches the ROI in size. Hence, embedding the coil just inside of a foam material will allow for increased filling factor and enable proper susceptibility matching, which results in maximum SNR and image quality. In addition, foams in general are ubiquitous in the MR suite. Foams are typically used as a cushion for patient comfort and to minimize patient movement during an experiment. Foam ear plugs are also ubiquitous for patient safety inside the scanner. Replacing regular ear plugs with PG foam ear plugs with the proper acoustic attenuation properties may even reduce susceptibility artifacts near the temporal lobe due to the air in the aural cavities.

5.4.4 Conclusions

Our results demonstrated that PG foam blocks and cushions removed magnetic susceptibility-induced field gradients near air-tissue interfaces, did not reduce the SNR in a receive coil, and improved the robustness of frequency selective fat suppression for both in phantoms and in the posterior neck. Field maps were acquired to generate field distribution histograms of the relevant ROIs. Critically, we showed here that the PG foam improves the field to the threshold (± 1 ppm) for robust fat suppression in 99% (from 44%) and 98% (from 84%) of the voxels in the fat phantom and in the posterior neck, respectively. These field maps demonstrated a *significant* improvement in static field homogeneity when the air-tissue interface was removed from the ROI by the PG foams. We have also introduced several potential clinical applications where the PG foams may increase SNR, contrast, and image quality. Further studies are required for each specific application to evaluate potential improvements from the use of PG foams, such as clinically prescribed T_1 and T_2 -weighted imaging, fat suppression in angiography as well as dynamic contrast enhanced breast cancer studies, BOLD fMRI, temperature monitoring for interventional MRI, and spectroscopy.

Chapter 6

Future Applications

6.1 Introduction

In this chapter, we present preliminary experiments that motivate potential future applications of the PG foam.

6.2 MRI in the Extremities

6.2.1 Motivation

MRI in the extremities, such as the hand or feet, can be difficult due to the irregularly shaped anatomies, which makes uniform static field homogeneity difficult to achieve (66). By wrapping the extremities in susceptibility matched PG foam, these field perturbations may be shifted away from the ROI. Foam padding is commonly used in the MR suite to suppress motion and to provide patient comfort, so extremity imaging is a natural application for PG foam. In addition, fat suppression is commonly used in extremity MRI to enhance contrast and PG foam should enable more robust fat saturation techniques.

6.2.2 Methods

3D casts of a hand and foot were made with a lifecasting system (Smooth-On, Easton, PA). Temporary negative molds were made with an alginate gel and filled with casting plaster to create detailed casts of the foot and hand. Sample hand and foot molds are shown in Fig 6.1. PG foams were casted around the molds in custom built plastic molding containers to create an ankle boot for the foot and a glove for the hand. 110 micron median diameter PG particles (Asbury Carbons, Asbury NJ) were disbursed into a closed-cell, two-component polyurethane polymer foam system (Silpak, Inc., Pomona, CA) to create the initial foam slurry. A custom plasticizer (Silpak, Inc., Pomona, CA) was also added both to reduce the viscosity of the initial foam slurry to facilitate homogeneous mixing and to create softer foams for patient comfort. The addition of the custom plasticizer modified the susceptibility of the base foam from minimally paramagnetic $\chi_{\text{Foam}} = \chi_{\text{Air}}$ to a slightly diamagnetic $\chi_{\text{Foam}} = -1$ ppm. We targeted foams with volume fraction $f = 3.9\%$ to match human tissue (or water) susceptibility of -9 ppm as before (Section 4.2.5).



Fig 6.1: Anatomical plaster molds of the hand and foot.

Sagittal 3D multi-slice gradient echo images of the foot were acquired with and without a PG foam ankle boot to produce off-resonance field maps from a 3T Siemens TRIO scanner (Siemens Medical Systems, Erlangen, Germany) using a standard Siemens field mapping pulse sequence and a standard head receive coil. A regular foam cushion was utilized as a control. The FOV of the 256x256 images was 25.6 x 25.6 cm² in-plane (1.0 x 1.0 mm² spatial resolution) with 3 mm slice thickness. Similar axial field maps were acquired of the hand. The field mapping sequence acquired a series of two similar 3D gradient echo scans with the same FOV to compute the off-resonance field maps. TR of both scans was 488 ms. TE was 4.92 and 7.38 ms for the two scans, respectively. A standard Siemens auto-shimming protocol including standard second order shims was used and the RF excitation pulse frequency was verified to be centered on the water peak for each case.

Standard T₁-weighted FLASH (Fast Low Angle Shot, a type of gradient echo sequence) images with and without frequency selective fat suppression were acquired to demonstrate the effect of field inhomogeneities with and without the use of PG foam ankle boot in the foot. The FOV of the 256x256 magnitude images was again 25.6 x 25.6 cm² in-plane (1.0 x 1.0 mm² spatial resolution) with 3 mm slice thickness. TR/TE of the gradient echo images was 589/2.46 ms. Identical auto-shimmed were prescribed as in the previous foot field maps.

6.2.3 Results

The prototype PG foam ankle boot, which does not cover the toes, is shown in Fig 6.2. Field maps of the foot demonstrate linear field perturbations without the use of the PG foam, which are homogenized inside the PG foam ankle boot (Fig. 6.3). Note the field perturbations that are generated at the new susceptibility boundary outside the ROI, which could be mitigated by extending the coverage of the PG foam boot. Figure 6.4 shows the failure of robust frequency selective fat suppression in the T₁-weighted FLASH images. Regions of failed fat suppression and unintentional tissue signal suppression are

clearly evident in the fat suppressed image with a normal cushion, but are not seen in the corresponding regions in the image acquired using the PG foam ankle boot. The prototype PG foam hand glove and corresponding field maps are shown in Fig 6.5. The PG foam homogenized the field inside the hand relative to the non-PG foam case.



Fig 6.2: PG foam ankle boot.

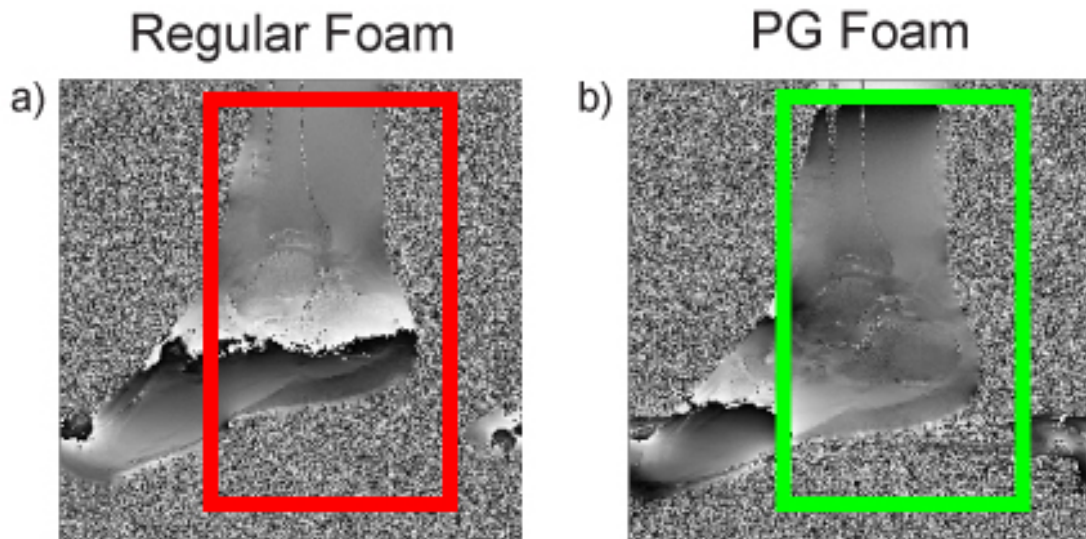


Fig 6.3: Regular and PG ankle boot field maps.

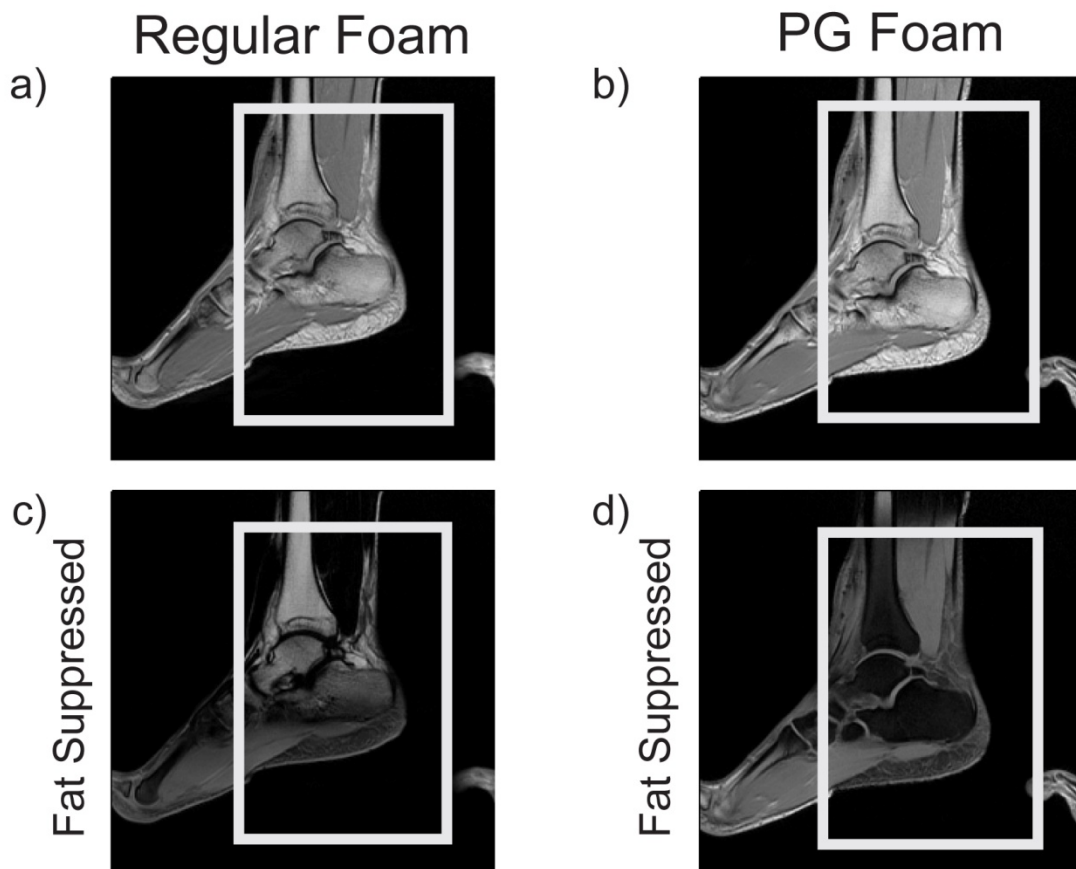


Fig 6.4: Improved fat suppression in the foot with PG foams.

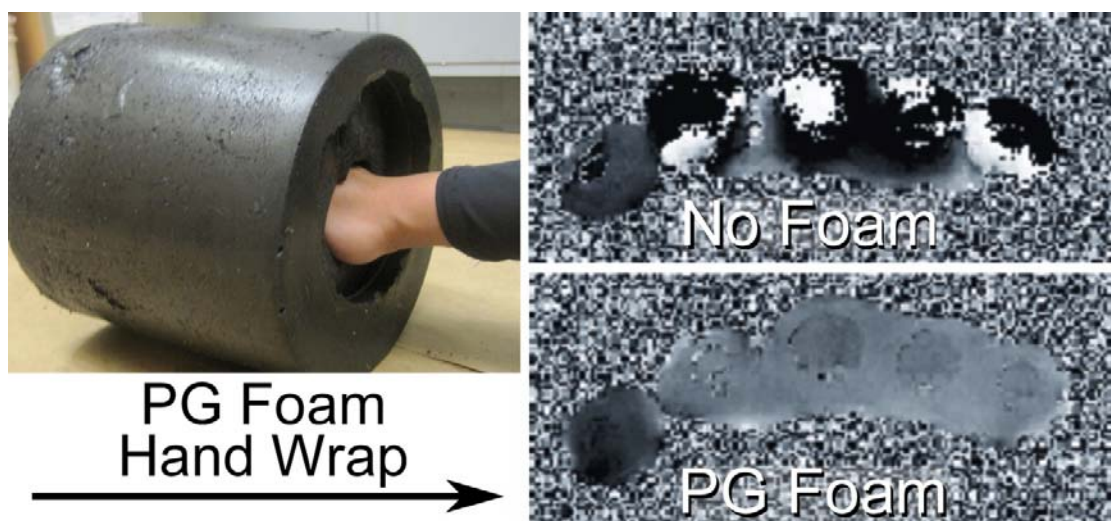


Fig 6.5: Improved field homogeneity in the hand with PG foams.

6.2.4 Brief Summary

Initial field maps demonstrate that the B_0 field in the foot and hand may be homogenized by the use of custom fitted PG foam wraps or cushions. PG foams also enabled more

robust frequency selective fat suppression in the foot. However, unlike a head or neck type of cushion, which can be manufactured in generic sizes, a conforming wrap for extremity MRI must be both more flexible and more closely fitted to the anatomy.

6.3 PG Foam Pellets

6.3.1 Motivation

Current PG foams are manufactured as pressure pads or cushions for regions of the body that are relatively similar or tolerant to repositioning across subjects, such as the head, neck, or breast. While PG foams are flexible and conforming to some degree, new techniques must be developed to realize the full susceptibility matching potential in harder to fit ROIs such as the foot, hand, knee, etc. One potential technique may be to reduce PG foams into small pellets which are free to move inside of a flexible, conforming cushion case or wrap. By shifting or compressing to fit the need of the relevant ROI, a more comfortable and conforming fit may be achieved.

6.3.2 Methods

PG foam blocks with volume fraction varying from 3.5 to 6% were made as before (Section 6.2). These blocks were hand cut to smaller pieces then ground into fine pellets with a standard kitchen blender. Previously built field map phantoms were filled with air, MnCl_2 -doped water, or PG foam pellets ($N = 4$ for each volume fraction) to create the relevant susceptibility boundaries.

Coronal 3T field maps of air, water, and PG foam phantoms were acquired on a Siemens scanner with a standard head coil as before (Section 4.2.3) to verify that the increase in PG foam configuration would have no effect of the target volume fraction for susceptibility matching. The field of view of the 256×256 field maps was $25.6 \times 25.6 \text{ cm}^2$ in-plane ($1.0 \times 1.0 \text{ mm}^2$ spatial resolution) with 3 mm slice thickness. The 3.5% PG foam pellets were then compressed to 9%, 20%, 32%, and 50% of their original volume and field mapped ($N = 4$) in order to investigate the effects of compression. Coronal 3D multi-slice EPI of the phantoms were acquired to observe the effects of the susceptibility induced field inhomogeneities on a long readout time pulse sequence. The FOV and slice thickness of the 64×64 images ($4.0 \times 4.0 \text{ mm}^2$ spatial resolution) were the same as the field maps. TR/TE of the EPI sequence was 2000/28 ms.

6.3.3 Results

An example of the PG foam pellets is shown in Fig 6.6. Fig 6.7 shows representative field maps of the range of uncompressed PG foams pellet phantoms. The field maps are depicted as unwrapped field maps to highlight any field perturbations. The dipole effect now inverts signs near the $f \sim 5.2\%$ PG pellet foams.



Fig 6.6: PG foam pellets.

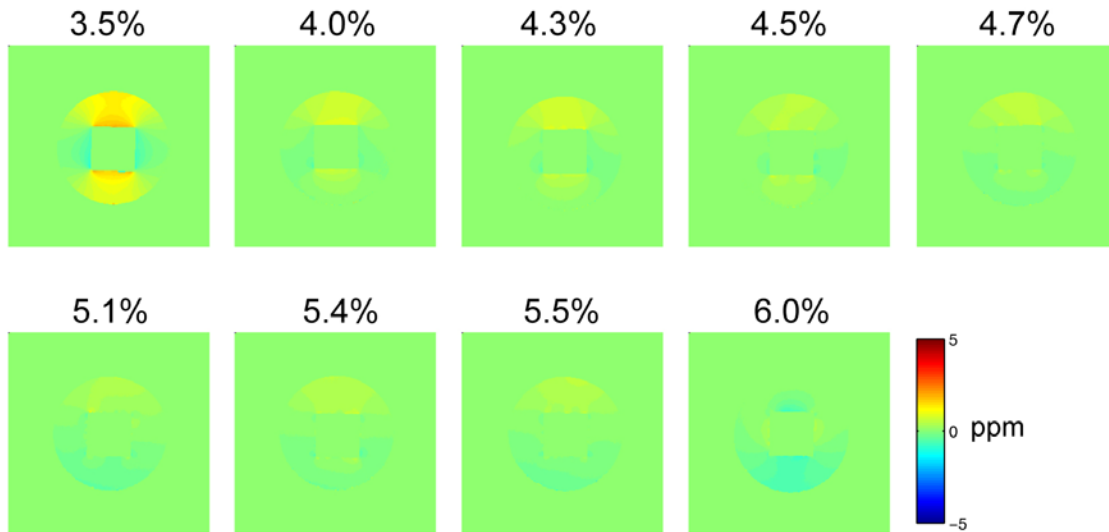


Fig 6.7: Experimental field maps of PG foam pellets with volume fractions ranging from 3.5% to 6%.

Fig 6.8 shows representative field maps and EPI images of the variably compressed 3.5% PG pellet phantoms. The dipole effect inverts signs between 32% and 50%, indicating that the compression increases the diamagnetic susceptibility of the pellet phantoms by reducing the volume, which in turn increases the volume fraction of PG. The corresponding EPI images also show that susceptibility artifacts are minimized at a level between 32% and 50% compression. The uneven signal dropouts on the square edges of the phantoms also suggest that the foams are not completely homogeneous as the solid PG foams used previously.

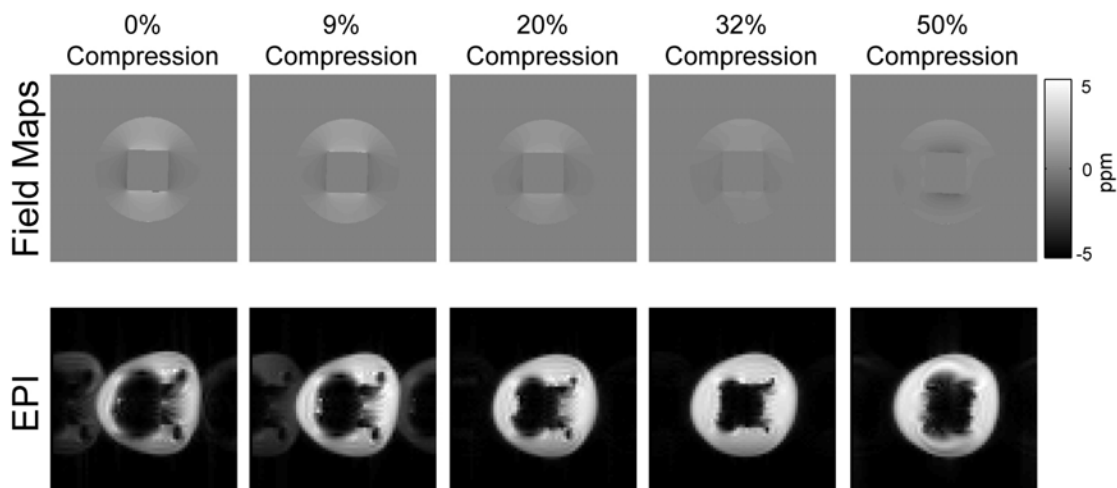


Fig 6.8: Experimental field maps and EPI images for 3.5% crumbs compressed to 0%, 9%, 20%, 32%, and 50% of the original volume.

6.3.4 Brief Summary

The prototype PG foam pellets offer increased conformability in the initial experiments. However, they are underdoped compared to the blocks from which they originated because the pellets allow for more air to be incorporated into the volume, i.e. the volume of the pellets can fluctuate depending on how the pellets settle. This suggests that managing the compression of the pellet based PG foam cushions will be a greater challenge compared to previous solid PG foams, which had 10% tolerances.

6.4 Industrial Manufacturing

6.4.1 Motivation

In addition to the target volume fraction for PG foams, homogeneous dispersal of the PG particles inside the foam is also important. While prototype PG foams were successfully manufactured and tested in house, large scale production of PG foams for future clinical applications and testing will rely on industrial engineering expertise to meet proper volume fraction and homogeneity criteria. To this end, we have collaborated with Mantec Services (Seattle, WA) to produce initial industrial PG foam prototypes.

6.4.2 Methods

Two sets of PG foam blocks with target volume fractions $\sim 1.5\%$ and $\sim 4.5\%$ were provided by Mantec Services, in addition to regular foams. The larger 100 micron particles were used, but the diamagnetic plasticizer was not. Mantec manufactured the PG foams to the target volume specifications provided using their own propriety processes. The Mantec samples were prepared for use with the previously built field map

phantoms, which were filled with either air, MnCl_2 -doped water, regular Mantec foams, or Mantec PG foam samples ($N = 4$ for each volume fraction) to create the relevant susceptibility boundaries.

Coronal 3T field maps of air, water, and Mantec PG foam phantoms were acquired on a Siemens scanner with a standard head coil as before (Section 4.2.3) to quantify passive susceptibility matching and to qualitatively observe the homogeneities of the test samples. The field of view of the 256×256 field maps was $25.6 \times 25.6 \text{ cm}^2$ in-plane ($1.0 \times 1.0 \text{ mm}^2$ spatial resolution) with 3 mm slice thickness.

6.4.3 Results

Several underdoped and regular prototype Mantec foams are shown in Fig 6.9. Fig 6.10 shows representative field maps of the $\sim 1.5\%$ Mantec PG foams phantoms compared to air and the regular foam phantoms. The field maps are depicted as unwrapped phase difference maps to highlight any field perturbations. The standard dipole effect is slightly reduced in the $\sim 1.5\%$ PG foams, but does not invert. Sigma (standard deviation) values of the Mantec foam induced field perturbations match those of the 1.5% Berkeley foams from Chapter 4.



Fig 6.9: Prototype Mantec foams in panel or cushion configuration.

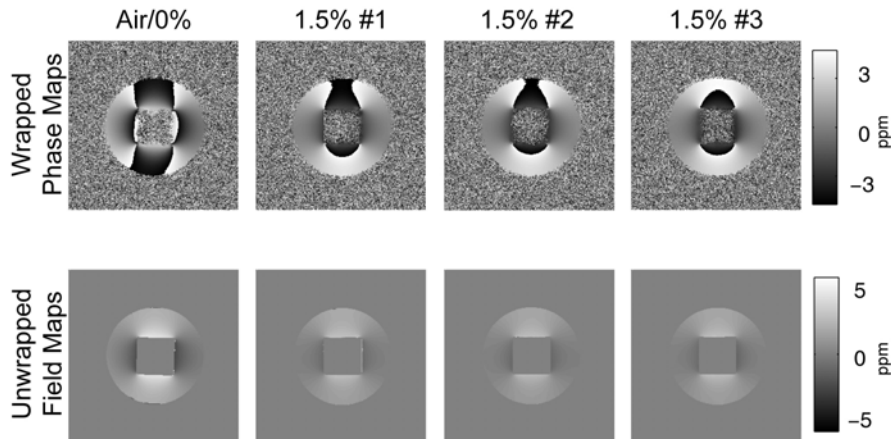


Fig 6.10: Experimental field maps of 1.5% volume fraction Mantec PG foams. Blocks from 3 separate samples were tested. The foams are underdoped, but have good homogeneity.

Fig 6.11 shows representative field maps of the 4.5% targeted Mantec PG foams. Some of the foams demonstrate susceptibility matching, but the bulk of the foams show uneven dipole effects, suggesting non-uniform volume fraction homogeneity. The few matched 4.5% Mantec PG foams have sigma values that match the 3.9% plasticizer-enhanced Berkeley PG foams.

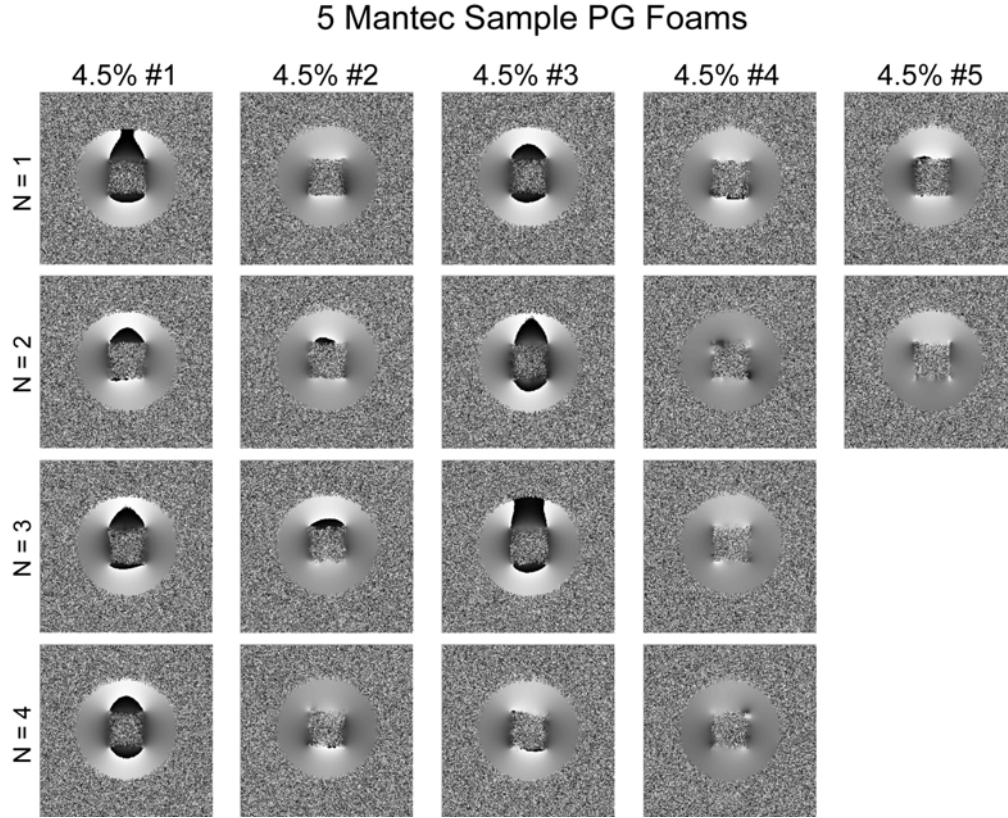


Fig 6.11: Experimental field maps of 4.5% volume fraction Mantec PG foams. Blocks from 5 separate samples were tested. The target volume fraction for susceptibility matching was achieved, but foam homogeneity was poor.

6.4.4 Brief Summary

The prototype Mantec PG foams demonstrate the possibility for outsourcing the large scale production of the susceptibility matching foams. Unfortunately, at larger foam volumes and higher volume fractions, it becomes increasingly difficult to manipulate the foam slurries. Methods to reduce the viscosity of the initial foam slurry and/or to reduce the target volume fraction required must be utilized. The custom plasticizer used in Chapter 4 may be one such way to improve the homogeneity of large scale, industrially produced PG foams. We will continue to test and validate new techniques.

6.5 Embedded RF Coils

Perhaps the most exciting feature of PG foam is the compatibility with embedded RF coils. In this thesis, the receiver coils used in the various PG foam experiments were not

optimized for the sample or subject. Because the coil resistance scales with the diameter of the coil and the sample resistance scales with the diameter of the coil to a power greater than one, SNR is increased by having the subject or sample at the same size of the coil (67). This is commonly known as the coil filling factor. By embedding an RF coil inside of a compatible susceptibility matching material such as PG foam, the finite thickness of PG foam required for removing external susceptibility-induced field perturbations can be excluded from the volume inside of the coil.

Two compelling examples for embedded RF coils are pediatric and breast MRI. clam shell body coils are often used for pediatric imaging, where minimizing acquisition speed and robust motion suppression are both important. In this particular application, the RF coil array may be sandwiched between a small layer of flexible or conforming PG foam on the subject side and more PG foam outside of the coil. Breast MRI, especially in conjunction with dynamic contrast enhancement, was previously discussed in this thesis. In addition to the use of modular breast specific receiver coils, specialized breast MRI (and biopsy compatible) tables are often used for imaging. One example is shown in Fig 6.12. Here we have designed prototype PG foams to fit into the breast imaging cavities which can both homogenize the field and suppress subject motion. The PG foams are also still compatible with biopsy with the additional use of a canula. PG foams can also enable repeatable positioning between patient scans. In conjunction with 3D modeled breast molds (Fig. 5.1) to generate an array of patient foam sizes and upcoming human subjects approval, we will have custom molded PG foams ready for proof of concept testing shortly.

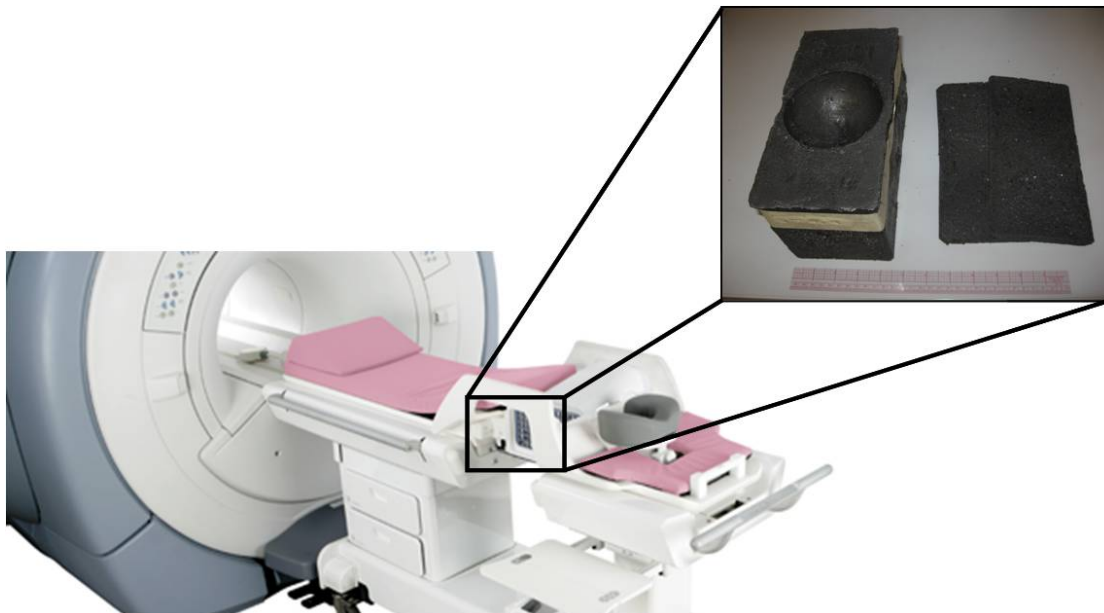


Fig 6.12: PG Foam compatible with Sentinelle Breast MRI Table (www.sentinellemedical.com).

Chapter 7

Summary and Future Work

7.1 Summary

The work presented in this thesis has focused on the development of PG foam for passive tissue magnetic susceptibility matching in MRI. The presented theory and imaging techniques have been analyzed with simulations and validated with phantom and *in vivo* proof of concept studies.

The contributions of this work to the field of MRI can be summarized as follows:

- Proposal of theory for calculating the bulk magnetic susceptibility for composite foams doped with a target volume fraction of highly anisotropic, diamagnetic PG particles. This theory predicts the ability to tailor the susceptibility of a flexible foam for passive susceptibility matching in MR studies.
- Application of effective medium theories to predict the electrical conductivities of the composite tissue susceptibility matching PG foams. This theory predicts that the PG foams will be nonconductive, will not heat, and is safe for patient use.
- Validation of bulk magnetic susceptibility theory and safety for the PG foams in phantom experiments. Proof of concept experiments demonstrate that passive tissue susceptibility matching PG foams for MRI can be used to homogenize the B_0 static field and minimize susceptibility induced artifacts.
- Demonstration of improved robustness of frequency selective fat suppression techniques through the use of the tissue susceptibility matching foam in phantoms and *in vivo*. Phantom simulations and experiments quantify improvements in the fat suppression. A volunteer study verifies the improvements in field homogeneity and in the reduction of susceptibility induced artifacts in fat suppressed T_1 -weighed images in the posterior neck and cervical spine.

7.2 Future Work

In this work, artifacts introduced by static field perturbations arising from heterogeneous susceptibility interfaces are alleviated by susceptibility matching composite PG foams, which homogenize the field near external air cavities. Many pulse sequences and techniques could benefit from a reliably uniform magnetic field provided by a

susceptibility matching material. Here we discuss EPI readouts for BOLD and Diffusion imaging, preventing banding artifacts from bSSFP sequences, robust fat suppression for cancer imaging, temperature monitoring for real-time monitoring of thermal ablation methods, and spectroscopic MRI.

For example, EPI sequences are known to suffer from signal dropout and distortion artifacts in regions of poor magnetic field homogeneity (28). EPI is the most popular pulse sequence used in blood oxygen level dependent (BOLD) functional MRI (fMRI) studies. BOLD fMRI contrast relies on the tiny susceptibility difference between oxygenated and deoxygenated hemoglobin (57). However, the BOLD effect can be unreliable in areas of strong field inhomogeneities. The PG neck cushions used in this study may be able to increase the robustness of fMRI studies, especially in the occipital lobe region or in the human spinal cord for motor tasks (68).

Diffusion weighted (DW) MRI generates diffusion contrast by balanced pulsed field gradient lobes. Any protons that have moved during the time interval between the pulses will not be refocused perfectly. This leads to a reduced signal that is related to the amount of diffusion. Unfortunately, static field gradients caused by air-tissue boundaries lead to T_2^* loss on that can degrade the diffusion contrast to noise ratio. 180° refocusing pulses are often used to mitigate T_2^* effects, but these can exceed Specific Absorption Rate (SAR) limitations, especially at higher field strengths.

For example, reduced FOV, single-shot EPI (ss-EPI) methods have recently been used for diffusion-weighted (DW) imaging to study and diagnose diseases arising from damage to the long fiber tracts of the spinal cord. A 2D spatially selective echo planar RF excitation pulse and a 180° refocusing pulse are used to reduce the FOV in the phase encode direction, while simultaneously suppressing fat (69). The reduction in readout time from the reduced FOV reduces the sensitivity to off-resonance effects, providing more robust ss-EPI DW images of the spinal cord. However, B_0 inhomogeneities result in geometric distortions near the edges of the excitation profile in the physical (axial) direction of the scanner along the spinal cord, resulting in failure of fat suppression in certain regions (69). Hence, reducing the field inhomogeneities in the posterior neck may enable proper fat suppression and more pristine diffusion contrast, which may result in more robust DW images of the spinal cord.

bSSFP pulse sequences achieve a steady state “spin echo-like” magnetization in which all gradient waveforms are refocused within each TR. This has greater SNR efficiency than spoiled steady state imaging methods (70). However, it is well-known that B_0 inhomogeneity (which is *not* refocused each TR) causes “banding” dropouts in the image where the dephasing $\theta = 2\pi \cdot \Delta B_{0, Hz} \cdot TR = \pm k\pi$, where k is an integer. To avoid banding artifacts in bSSFP imaging, it is critical to minimize both TR and field perturbations. For example, TR must be less than 1.6 ms to avoid banding artifacts for field perturbations of $\Delta B_{0, Hz} = \pm 320$ Hz at 1.5 T (± 5 ppm). At 3.0 T, TR must be twice as short (800 microseconds) to tolerate the same field inhomogeneity. However, both peripheral nerve stimulation limits (dB/dt) and amplitude limits (40 mT/m for modern gradient systems) make it extremely difficult, if not impossible, to achieve such a short

TR in high-resolution MRI. PG foam, which can reduce field inhomogeneity down to ± 1 ppm, would allow for 5 times longer bSSFP readouts, or 4 ms at 3.0 T. This would allow for very high spatial resolution, or it would allow for excellent resolution with no banding artifacts.

Dynamic contrast-enhanced MRI (DCE-MRI) is often used for diagnosing and staging cancer (71,72) with Gadolinium-based contrast agents. Unfortunately, fat has similar T_1 to blood with gadolinium contrast. Hence, fat can obscure tumors or DCE-MRI vessels or tumors in T_1 -weighted pulse sequences. Clearly one cannot use STIR pulse sequences with gadolinium contrast, since fat suppression would also suppress blood. Robust fat saturation in the presence of contrast agents then requires very uniform fields to perform chemical-shift selective fat suppression. Perhaps the most compelling application of PG foam is to improve fat suppression during DCE-MRI in the breast. Here the external field distortion is a significant contributor to the overall magnetic distortion. We are experimenting with conformable foams that retain susceptibility matching properties. In addition to homogenizing the field for fat suppressed DCE-MRI, shaped foams also ensure motion suppression and repeatable positioning between followup scans designed to monitor suspicious lesions growth.

MR Spectroscopic imaging is another clinical application that would greatly benefit from susceptibility matching materials. MRS has recently been used as a complementary study for the diagnosis of patients with prostate cancer or disease (59). A susceptibility matched barium sulfate solution, replacing air, has been applied successfully to inflate an endorectal coil for 3T MRS of the prostate, resulting in reduced susceptibility field gradients and a corresponding narrowing of metabolite peaks, which is crucial to resolve the peaks of closely spaced metabolites such as choline and citrate, which are 0.55 ppm apart. (40). In addition, water suppression is typically used in MRS to better observe other metabolites because water is the dominant chemical species in the body. PG foams may be practical for improving MRS, especially in regions of abrupt field variations, including the breast, neck, brain, and spine.

Proton resonant frequency shift (PRF) MR thermometry techniques have become invaluable for monitoring minimally invasive thermal therapies such as high-intensity focused ultrasound (HIFU) or RF ablation (60). PRF-based temperature mapping requires stringent field uniformity since the PRF shift is only 0.010 ppm/ $^{\circ}\text{C}$. Moreover, it is helpful to suppress fat when using MR thermometry. MRI compatible HIFU probes have been developed (73), but they have not yet been integrated with a susceptibility-matching agent like PG foam.

In this thesis, a passive tissue magnetic susceptibility matching PG foam was theorized, developed, and validated in phantom and in the posterior neck and cervical spine of volunteers. Future work includes developing techniques to improve the material properties of the foam and conducting proof of concept experiments to validate potential B_0 -sensitive MR applications and techniques that will benefit from reductions in static field gradients.

Bibliography

1. Kalorama Information, 2009.
2. Haacke EM. Magnetic Resonance Imaging: Physical Principles and Sequence Design. New York: Wiley; 1999. xxvii, 914 p. p.
3. Nishimura DG. Principles of Magnetic Resonance Imaging: www.lulu.com; 2010.
4. Rabi II, Zacharias JR, Millman S, Kusch P. A New Method of Measuring Nuclear Magnetic Moment. Physical Review 1938;53(4):318-318.
5. Bloch F. Nuclear Induction. Physical Review 1946;70(7-8):460-474.
6. Purcell EM, Torrey HC, Pound RV. Resonance Absorption by Nuclear Magnetic Moments in a Solid. Physical Review 1946;69(1-2):37-38.
7. Lauterbur PC. Image Formation by Induced Local Interactions: Examples Employing Nuclear Magnetic Resonance. Nature 1973;242(5394):190-191.
8. Mansfield P. NMR 'Diffraction' in Solids? J Chem Phys 1973;58(4):1772.
9. Schenck JF. The role of magnetic susceptibility in magnetic resonance imaging: MRI magnetic compatibility of the first and second kinds. Medical Physics 1996;23(6):815-850.
10. Koch KM, Rothman DL, de Graaf RA. Optimization of static magnetic field homogeneity in the human and animal brain in vivo. Prog Nucl Magn Reson Spectrosc 2009;54(2):69-96.
11. Jenkinson M. Fast, automated, N-dimensional phase-unwrapping algorithm. Magn Reson Med 2003;49(1):193-197.
12. Pappis J, Blum SL. Properties of Pyrolytic Graphite. Journal of the American Ceramic Society 1961;44(12):592-597.
13. Slack GA. Anisotropic Thermal Conductivity of Pyrolytic Graphite. Physical Review 1962;127(3):694.
14. Hirono S, Umemura S, Tomita M, Kaneko R. Superhard conductive carbon nanocrystallite films. Applied Physics Letters 2002;80(3):425-427.
15. Tarling DH, Hrouda F. The Magnetic Anisotropy of Rocks. London ; New York: Chapman & Hall; 1993.
16. Jelínek V, Kropáček V. Statistical processing of anisotropy of magnetic susceptibility measured on groups of specimens. Studia Geophysica Et Geodaetica 1978;22(1):50-62.
17. Chen CN, Hoult DI. Biomedical Magnetic Resonance Technology. Bristol: Adam Hilger; 2005.
18. Johnson CC, Guy AW. Nonionizing electromagnetic wave effects in biological materials and systems. Proceedings of the IEEE 1972;60(6):692-718.
19. McLachlan DS, Blaszkiewicz M, Newnham RE. Electrical Resistivity of Composites. Journal of the American Ceramic Society 1990;73(8):2187-2203.
20. McLachlan DS, Cai K, Sauti G. AC and dc conductivity-based microstructural characterization. International Journal of Refractory Metals and Hard Materials 2001;19(4-6):437-445.

21. Brady S, Diamond D, Lau K-T. Inherently conducting polymer modified polyurethane smart foam for pressure sensing. *Sensors and Actuators A: Physical* 2005;119(2):398-404.
22. Chen P, Wu RX, Zhao T, Yang F, Xiao JQ. Complex permittivity and permeability of metallic magnetic granular composites at microwave frequencies. *Journal of Physics D: Applied Physics* 2005;38(14):2302-2305.
23. Inan U, Inan A. *Electromagnetic Theory*. Menlo Park, CA: Addison-Wesley; 1999. xx, 747 p. p.
24. Bottomley PA, Edelstein WA. Power deposition in whole-body NMR imaging. *Med Phys* 1981;8(4):510-512.
25. Reilly JP. Peripheral nerve stimulation by induced electric currents: exposure to time-varying magnetic fields. *Med Biol Eng Comput* 1989;27(2):101-110.
26. Schaefer DJ. Safety aspects of radiofrequency power deposition in magnetic resonance. *Magn Reson Imaging Clin N Am* 1998;6(4):775-789.
27. Chou CK, Bassen H, Osepchuk J, Balzano Q, Petersen R, Meltz M, Cleveland R, Lin JC, Heynick L. Radio frequency electromagnetic exposure: tutorial review on experimental dosimetry. *Bioelectromagnetics* 1996;17(3):195-208.
28. Jezzard P, Balaban RS. Correction for geometric distortion in echo planar images from B0 field variations. *Magnetic Resonance in Medicine* 1995;34(1):65-73.
29. Jezzard P, Clare S. Sources of distortion in functional MRI data. *Human Brain Mapping* 1999;8(2-3):80-85.
30. Dixon WT. Simple proton spectroscopic imaging. *Radiology* 1984;153(1):189-194.
31. Blamire AM, Rothman DL, Nixon T. Dynamic shim updating: A new approach towards optimized whole brain shimming. *Magnetic Resonance in Medicine* 1996;36(1):159-165.
32. Schneider E, Glover G. Rapid in vivo proton shimming. *Magnetic Resonance in Medicine* 1991;18(2):335-347.
33. Wilson JL, Jenkinson M, de Araujo I, Kringelbach ML, Rolls ET, Jezzard P. Fast, Fully Automated Global and Local Magnetic Field Optimization for fMRI of the Human Brain. *Neuroimage* 2002;17(2):967-976.
34. Wilson JL, Jenkinson M, Jezzard P. Optimization of static field homogeneity in human brain using diamagnetic passive shims. *Magnetic Resonance in Medicine* 2002;48(5):906-914.
35. Wilson JL, Jenkinson M, Jezzard P. Protocol to determine the optimal intraoral passive shim for minimisation of susceptibility artifact in human inferior frontal cortex. *Neuroimage* 2003;19(4):1802-1811.
36. Wilson JL, Jezzard P. Utilization of an intra-oral diamagnetic passive shim in functional MRI of the inferior frontal cortex. *Magn Reson Med* 2003;50(5):1089-1094.
37. Hsu JJ, Glover GH. Mitigation of susceptibility-induced signal loss in neuroimaging using localized shim coils, *Magn Reson Med* 2005;53:243-248. *Magnetic Resonance in Medicine* 2005;53(4):992.
38. Juchem C, Nixon TW, McIntyre S, Rothman DL, Graaf RAd. Magnetic field homogenization of the human prefrontal cortex with a set of localized electrical coils. *Magnetic Resonance in Medicine* 2009;63(1):171-180.

39. Eilenberg SS, Tartar VM, Mattrey RF. Reducing Magnetic-Susceptibility Differences Using Liquid Fluorocarbon Pads (Sat Pad(Tm)) - Results with Spectral Presaturation of Fat. Artificial Cells Blood Substitutes and Immobilization Biotechnology 1994;22(4):1477-1483.
40. Rosen Y, Bloch BN, Lenkinski RE, Greenman RL, Marquis RP, Rofsky NM. 3T MR of the prostate: Reducing susceptibility gradients by inflating the endorectal coil with a barium sulfate suspension. Magnetic Resonance in Medicine 2007;57(5):898-904.
41. Mitchell DG, Vinitski S, Mohamed FB, Mammone JF, Haidet K, Rifkin MD. Comparison of Kaopectate with barium for negative and positive enteric contrast at MR imaging. Radiology 1991;181(2):475-480.
42. Bhagwandien R, Moerland MA, Bakker CJG, Beersma R, Lagendijk JJW. Numerical analysis of the magnetic field for arbitrary magnetic susceptibility distributions in 3D. Magnetic Resonance Imaging 1994;12(1):101-107.
43. Yoshimura K, Kato H, Kuroda M, Yoshida A, Hanamoto K, Tanaka A, Tsunoda M, Kanazawa S, Shibuya K, Kawasaki S, Hiraki Y. Development of a tissue-equivalent MRI phantom using carrageenan gel. Magnetic Resonance in Medicine 2003;50(5):1011-1017.
44. Maril N, Collins CM, Greenman RL, Lenkinski RE. Strategies for shimming the breast. Magnetic Resonance in Medicine 2005;54(5):1139-1145.
45. Gilbert KM, Scholl TJ, Chronik BA. RF coil loading measurements between 1 and 50 MHz to guide field-cycled MRI system design. Concepts in Magnetic Resonance Part B: Magnetic Resonance Engineering 2008;33B(3):177-191.
46. Koch KM, Papademetris X, Rothman DL, Graaf RAd. Rapid calculations of susceptibility-induced magnetostatic field perturbations for in vivo magnetic resonance. Physics in Medicine and Biology 2006(24):6381.
47. Sardanelli F, Schiavoni S, Iozzelli A, Fausto A, Aliprandi A, Mancardi G, Filippi M. The value of chemical fat-saturation pulse added to T1-weighted spin-echo sequence in evaluating gadolinium-enhancing brain lesions in multiple sclerosis. La Radiologia Medica 2007;112(8):1244-1251.
48. Keller P, Hunter W, Jr, Schmalbrock P. Multisection fat-water imaging with chemical shift selective presaturation. Radiology 1987;164(2):539-541.
49. de Kerviler E, Leroy-Willig A, Clément O, Frija J. Fat suppression techniques in MRI: An update. Biomedecine & Pharmacotherapy 1998;52(2):69-75.
50. Delfaut EM, Beltran J, Johnson G, Rousseau J, Marchandise X, Cotten A. Fat Suppression in MR Imaging: Techniques and Pitfalls. Radiographics 1999;19(2):373-382.
51. Glover GH. Multipoint dixon technique for water and fat proton and susceptibility imaging. Journal of Magnetic Resonance Imaging 1991;1(5):521-530.
52. Wohlgemuth W, Roemer F, Bohndorf K. Short tau inversion recovery and three-point Dixon water-fat separation sequences in acute traumatic bone fractures at open 0.35 tesla MRI. Skeletal Radiology 2002;31(6):343-348.
53. Barger AV, DeLone DR, Bernstein MA, Welker KM. Fat Signal Suppression in Head and Neck Imaging Using Fast Spin-Echo-IDEAL Technique. AJNR Am J Neuroradiol 2006;27(6):1292-1294.

54. Marques JP, Bowtell R. Application of a Fourier-based method for rapid calculation of field inhomogeneity due to spatial variation of magnetic susceptibility. *Concepts in Magnetic Resonance Part B: Magnetic Resonance Engineering* 2005;25B(1):65-78.
55. Salomir R, Denis de Senneville B, Moonen CT. A fast calculation method for magnetic field inhomogeneity due to an arbitrary distribution of bulk susceptibility. *Concepts in Magnetic Resonance Part B: Magnetic Resonance Engineering* 2003;19B(1):26-34.
56. Meyer CH, Pauly JM, Macovski A, Nishimura DG. Simultaneous spatial and spectral selective excitation. *Magn Reson Med* 1990;15(2):287-304.
57. Ogawa S, Lee TM, Kay AR, Tank DW. Brain magnetic resonance imaging with contrast dependent on blood oxygenation. *Proc Natl Acad Sci U S A* 1990;87(24):9868-9872.
58. Peh WC, Chan JH. Artifacts in musculoskeletal magnetic resonance imaging: identification and correction. *Skeletal Radiol* 2001;30(4):179-191.
59. Kurhanewicz J, Swanson MG, Nelson SJ, Vigneron DB. Combined magnetic resonance imaging and spectroscopic imaging approach to molecular imaging of prostate cancer. *J Magn Reson Imaging* 2002;16(4):451-463.
60. Rieke V, Butts Pauly K. MR thermometry. *J Magn Reson Imaging* 2008;27(2):376-390.
61. Lee GC, Goodwill PW, Phuong K, Inglis BA, Scott GC, Hargreaves BA, Li L, Chen AC, Shah RN, Conolly SM. Pyrolytic graphite foam: a passive magnetic susceptibility matching material. *J Magn Reson Imaging* 2009;32(3):684-691.
62. Constantinides CD, Atalar E, McVeigh ER. Signal-to-noise measurements in magnitude images from NMR phased arrays. *Magn Reson Med* 1997;38(5):852-857.
63. Jordan CD, Daniel BL, Koch KM, Yu H, Conolly S, Hargreaves B. Validation of susceptibility-based models with field map measurements in the breast. *Proc 19th ISMRM* 2011 2011.
64. Spottiswoode B. <http://www.mathworks.com/matlabcentral/fileexchange/22504>. 2008.
65. Lauenstein TC, Sharma P, Hughes T, Heberlein K, Tudorascu D, Martin DR. Evaluation of optimized inversion-recovery fat-suppression techniques for T2-weighted abdominal MR imaging. *J Magn Reson Imaging* 2008;27(6):1448-1454.
66. Mirowitz SA. Fast scanning and fat-suppression MR imaging of musculoskeletal disorders. *AJR Am J Roentgenol* 1993;161(6):1147-1157.
67. Roemer PB, Edelstein WA, Hayes CE, Souza SP, Mueller OM. The NMR phased array. *Magn Reson Med* 1990;16(2):192-225.
68. Maieron M, Iannetti GD, Bodurka J, Tracey I, Bandettini PA, Porro CA. Functional responses in the human spinal cord during willed motor actions: evidence for side- and rate-dependent activity. *J Neurosci* 2007;27(15):4182-4190.
69. Saritas EU, Cunningham CH, Lee JH, Han ET, Nishimura DG. DWI of the spinal cord with reduced FOV single-shot EPI. *Magn Reson Med* 2008;60(2):468-473.
70. Scheffler K, Lehnhardt S. Principles and applications of balanced SSFP techniques. *Eur Radiol* 2003;13(11):2409-2418.

71. Hylton N. Dynamic contrast-enhanced magnetic resonance imaging as an imaging biomarker. *J Clin Oncol* 2006;24(20):3293-3298.
72. Yamashita Y, Mitsuzaki K, Ogata I, Takahashi M, Hiai Y. Three-dimensional high-resolution dynamic contrast-enhanced MR angiography of the pelvis and lower extremities with use of a phased array coil and subtraction: diagnostic accuracy. *J Magn Reson Imaging* 1998;8(5):1066-1072.
73. Wong SH, Watkins RD, Kupnik M, Pauly KB, Khuri-Yakub BT. Feasibility of MR-temperature mapping of ultrasonic heating from a CMUT. *Ultrasonics, Ferroelectrics and Frequency Control, IEEE Transactions on* 2008;55(4):811-818.